

Mechanochemical bistability of intestinal organoids enables robust morphogenesis

Received: 4 July 2023

Accepted: 16 January 2025

Published online: 28 February 2025

Shi-Lei Xue^{1,2,10}, Qiutan Yang^{3,4,5,6,7,8,10}, Prisca Liberali^{3,9} ✉ & Edouard Hannezo² ✉

Reproducible pattern and form generation during embryogenesis is poorly understood. Intestinal organoid morphogenesis involves a number of mechanochemical regulators such as cell-type-specific cytoskeletal forces and osmotically driven lumen volume changes. It is unclear how these forces are coordinated in time and space to ensure robust morphogenesis. Here we show how mechanosensitive feedback on cytoskeletal tension gives rise to morphological bistability in a minimal model of organoid morphogenesis. In the model, lumen volume changes can impact the epithelial shape via both direct mechanical and indirect mechanosensitive mechanisms. We find that both bulged and budded crypt states are possible and dependent on the history of volume changes. We test key modelling assumptions via biophysical and pharmacological experiments to demonstrate how bistability can explain experimental observations, such as the importance of the timing of lumen shrinkage and robustness of the final morphogenetic state to mechanical perturbations. This suggests that bistability arising from feedback between cellular tensions and fluid pressure could be a general mechanism that coordinates multicellular shape changes in developing systems.

Embryos are sculpted by a variety of physical forces^{1–3}, such as active tensions from the cellular cytoskeleton⁴, and compressive stresses from external physical constraints or differential tissue growth^{5–10}. Furthermore, hydrostatic pressure forces are emerging as important regulators for supracellular morphogenesis^{11–22}. Although physical forces play key functional roles during morphogenesis, it is still unclear whether and how they are coordinated with each other and with concomitant biochemical signalling events, such as morphogen gradients and cell fate specification^{23–26}. Indeed, cells and tissues typically experience large noise, both at the biochemical and mechanical levels, begging the question of how morphogenesis can occur in a reproducible manner^{27–34}.

The development of the vertebrate intestine represents a prototypical example of a complex morphogenetic sequence resulting in a highly stereotypical folded configuration, which is necessary to supply an adequate surface area for nutrient absorption^{8,9}. The epithelium of the small intestine is organized in a folded monolayer with highly curved invaginations (crypts), where stem cells reside, and large finger-like protrusions (villi) into the intestinal lumen consisting of differentiated cells^{9,35}. To overcome the limited accessibility of internal tissues, intestinal organoids have emerged as an ideal in vitro self-organized model system amenable to live imaging and mechanochemical perturbations^{22,36–38}, particularly as organoid crypts display similar shapes and cell fates as their in vivo

¹Department of Materials Science and Engineering, School of Engineering, Westlake University, Hangzhou, China. ²Institute of Science and Technology Austria, Klosterneuburg, Austria. ³Friedrich Miescher Institute for Biomedical Research (FMI), Basel, Switzerland. ⁴State Key Laboratory of Stem Cell and Reproductive Biology, Institute of Zoology, Chinese Academy of Sciences, Beijing, China. ⁵Institute for Stem Cell and Regeneration, Chinese Academy of Sciences, Beijing, China. ⁶Beijing Institute for Stem Cell and Regenerative Medicine, Beijing, China. ⁷University of Chinese Academy of Sciences, Beijing, China. ⁸Key Laboratory of Organ Regeneration and Reconstruction, Chinese Academy of Sciences, Beijing, China. ⁹University of Basel, Basel, Switzerland. ¹⁰These authors contributed equally: Shi-Lei Xue, Qiutan Yang. ✉ e-mail: prisca.liberali@fmi.ch; edouard.hannezo@ist.ac.at

counterparts^{37,39} (Extended Data Fig. 1a–e). Organoid morphogenesis is organized by fate-dependent forces from the crypt and villi regions, actomyosin-driven apical constriction and lumen osmotic forces^{22,36,40} (Fig. 1a,b, Extended Data Fig. 1 and Supplementary Video 1).

However, whether these two key mechanical events are independently regulated or intrinsically coupled at the level of an entire organoid remains unclear. For instance, in our previous modelling, lumen deflation accelerates crypt budding, but is not strictly necessary for budding as long as apical actomyosin constriction is large enough. This is consistent with our previous data showing that budded crypts have morphologies robust to lumen volume increase²². Nevertheless, this does not explain our experimental observation that lumen volume reduction at the onset of morphogenesis is required for crypt budding (Fig. 1a–d, Extended Data Figs. 2 and 3 and Supplementary Videos 1–3). From a more conceptual level, this hints at the non-intuitive idea that the timing of a given mechanical event critically modulates its morphogenetic impact, with the same change in lumen volume giving rise to completely different outcomes if performed before or after crypt budding, despite similar cell fate compositions (Extended Data Fig. 1a–e). Such feature, not captured by current theoretical models, could act as a source of robustness for morphogenesis, as it would result in the crypt shape being both sensitive to mechanical forces during morphogenesis and insensitive to mechanical fluctuations once morphogenesis is completed.

Here we propose a biophysical theory for the coordination and robustness of mechano-osmotic forces driving intestinal organoid morphogenesis. Via an analytically tractable three-dimensional (3D) vertex model, we find that the phase diagram for organoid morphologies contains a mechanically bistable region: both open (bulged) and closed (budded) crypt configurations are possible for a specific organoid volume, and the ultimate morphological outcome depends on the history of the system. Biochemical bistability has been proposed as a key source of robustness for stem cell fate determination by allowing cells to both commit to a given fate on an inducing signal and retain this fate even after the signal has been removed^{41,42}. We hypothesized that lumen pressure could play the role of an inducing signal in multicellular systems, with mechanical bistability resulting in organoid shape being both (1) tightly controlled by lumen pressure during morphogenesis and (2) highly insensitive to mechanical changes once morphogenesis is complete (Fig. 1a,e). We also find that the regime of parameters allowing for bistability is drastically enhanced by considering a mechanosensitive coupling between actomyosin tension and lumen pressure, which we verified experimentally and allowed us to quantitatively recapitulate organoid morphogenesis and various perturbations.

Theory of bistable crypt morphology controlled by lumen volume

We theoretically describe an intestinal organoid as a closed epithelial monolayer with two different regions—crypt and villus—which encapsulates an incompressible fluid lumen. We have previously shown that such a two-region 3D vertex model, which captures the effects of cell-scale active forces on tissue-scale deformation, can accurately predict organoid morphologies²². In the model, we consider a single cell with three surface tensions Γ_a , Γ_b and Γ_l , arising from cell–cell adhesion and actomyosin-induced tension along the cell membrane^{43–46}, and three surface areas A_a , A_b and A_l , with subscripts a, b and l representing the apical, basal and lateral surfaces/domains, respectively (Fig. 2a). Then, the free energy of a single cell reads

$$f = \Gamma_a A_a + \Gamma_b A_b + \frac{1}{2} \Gamma_l A_l.$$

When considering that the crypt and villus regions can each have different mechanical properties, the possible morphologies of an organoid depend on four dimensionless parameters (Supplementary

Note 1.1): (1) the relative size of the crypt ϕ (that is, the ratio of the number of crypt cells to the total number); (2) normalized organoid volume v ; (3) in-plane tension ratio $\alpha = \frac{(\Gamma_a + \Gamma_b)_c}{(\Gamma_a + \Gamma_b)_v}$ (with the subscripts c and v denoting the crypt and villus tissues, respectively); and (4) differential tension between the apical and basal sides of the crypt cells $\sigma_c = \frac{1}{2} \left(\frac{\Gamma_a - \Gamma_b}{\Gamma_l} \right)_c \sqrt{\frac{4\pi}{N_c}}$ (with N_c being the total number of cells in the organoid), which causes the crypt cells to have a preferred curvature.

Previously, we considered apical myosin in crypts as the key parameter²², which changes both in-plane tension α and differential tension σ_c . However, more complex regulatory patterns of myosin can be observed experimentally, including basal crypt actomyosin relocation during lumen inflation (Extended Data Fig. 1f and Supplementary Video 4). When theoretically investigating the separate consequences of differential tension σ_c and in-plane tension α , we found that in specific regions of the phase diagram (Fig. 2a), crypt morphology can show two stable configurations (either open or closed shape) for the same lumen volume and, thus, display morphological bistability. To gain insights into this theoretical phenomenon, we consider the limit of large lumen volume, for which the dependency of the total mechanical energy⁴⁷ of the organoid on the crypt shape (represented by crypt opening angle θ_c) can be derived analytically:

$$\Delta F(x) = \left[1 - \sigma_c \left(\frac{1+x}{2\phi} \right)^{\frac{1}{2}} \right]^{\frac{2}{3}} \left(1 - \frac{1-x}{2\alpha} \right)^{\frac{1}{3}},$$

where $x = \cos(\theta_c)$. Depending on differential tension σ_c , three scenarios exist (Fig. 2b and Extended Data Fig. 4): (1) for small σ_c , the crypt epithelium will stay open/bulged; (2) for intermediate differential tension σ_c , two local energy minima exist, indicating that both open and closed configurations are possible; (3) for large enough σ_c , the crypt will always be budded. Next, we look at the morphological evolution of the organoid shape on lumen volume change. The ‘degree of crypt opening’, described as $\theta_c/(\pi - \theta_c)$, is used to quantify the crypt morphology (Figs. 1 and 2c and Extended Data Fig. 2), ranging from 0 to 1, with 0 standing for the budded shape (with the crypt and villus fully closed) and 1 for a spherical organoid. For small differential tension (for example, $\sigma_c = 0.1$), crypt morphology evolves continuously and monotonously with changes in the lumen volume: the crypt opens (or closes) on lumen inflation (or shrinkage) (characterized by path A→D). With intermediate differential tension (for example, $\sigma_c = 0.15$), the crypt gradually closes up with lumen shrinkage until fully closed; however, the morphological evolution is no longer reversible as this closed crypt cannot be opened by further volume inflation (path B→C).

Such morphological hysteresis—or path-dependent evolution—is a classical feature of bistable systems⁴¹, and is qualitatively consistent with our data (Fig. 1). Starting from a bulged/open crypt, increasing the differential tension at a constant volume drives an entry into the bistable region from the ‘bulged’ configuration. Therefore, crypts are prone to stay bulged (path A→C)—mirroring our data that impairing volume decrease during morphogenesis (day 3 to day 4) impairs crypt budding (Fig. 1c and Supplementary Video 2). By contrast, if the differential tension increases at the same time as the decrease in lumen volume (path A→B), organoids can reach the monostable budded state, consistent with our data on normal organoid morphogenesis (Fig. 1b and Supplementary Video 1). Crucially, the subsequently increasing lumen volume back to its initial value once crypts are already budded (path B→C) results in organoids entering the bistable region from the ‘budded’ configuration and, thus, remain in this state, as in our inflation data (Fig. 1d and Supplementary Video 3), despite reaching the same final volume as in the first path (A→C).

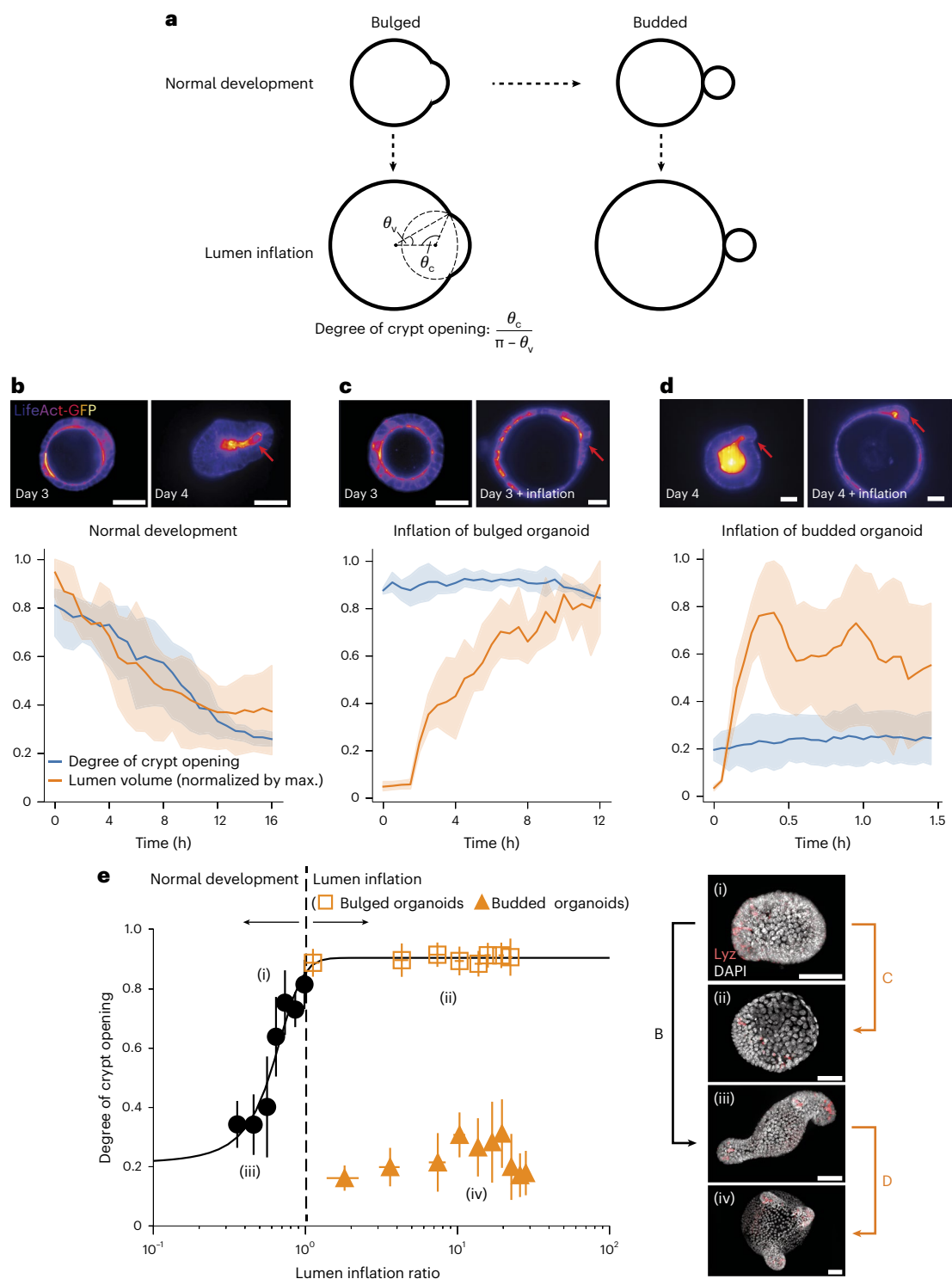


Fig. 1 | Crypt morphology depends on lumen volume changes in a history-dependent manner. **a**, Cartoon representation of normal and mechanically perturbed crypt morphogenesis. **b–d**, Top, representative time-lapse recordings of the normal development (**b**) of intestinal organoids, as well as the lumen inflation (performed by PGE treatment) of both bulged (**c**) and budded (**d**) organoids. Bottom, corresponding degree of crypt opening and lumen volume (normalized by the maximum value) as a function of time (number of samples $N = 4$ in each scenario). The solid lines represent the mean values and the shaded regions represent the 95% confidence intervals. **e**, Left, bistable relationship

between the degree of crypt opening and lumen inflation ratio: early lumen inflation (**c**; (i)→(ii)) impairs long-term crypt budding morphogenesis, whereas lumen inflation after normal development (**d**; (iii)→(iv)) has negligible effect (number of samples $N = 4$ in each scenario). Data are presented as mean values \pm s.d. Right, representative snapshots of four types of crypt state: (i) day 3.5 bulged organoid; (ii) day 4 organoid that remained bulged due to long-term lumen inflation; (iii) day 4 budded organoid (unperturbed); and (iv) day 4 budded organoid after lumen inflation. Images are the maximum z projections of the organoids with DAPI and Lyz staining. Scale bars, 50 μm (**b–e**).

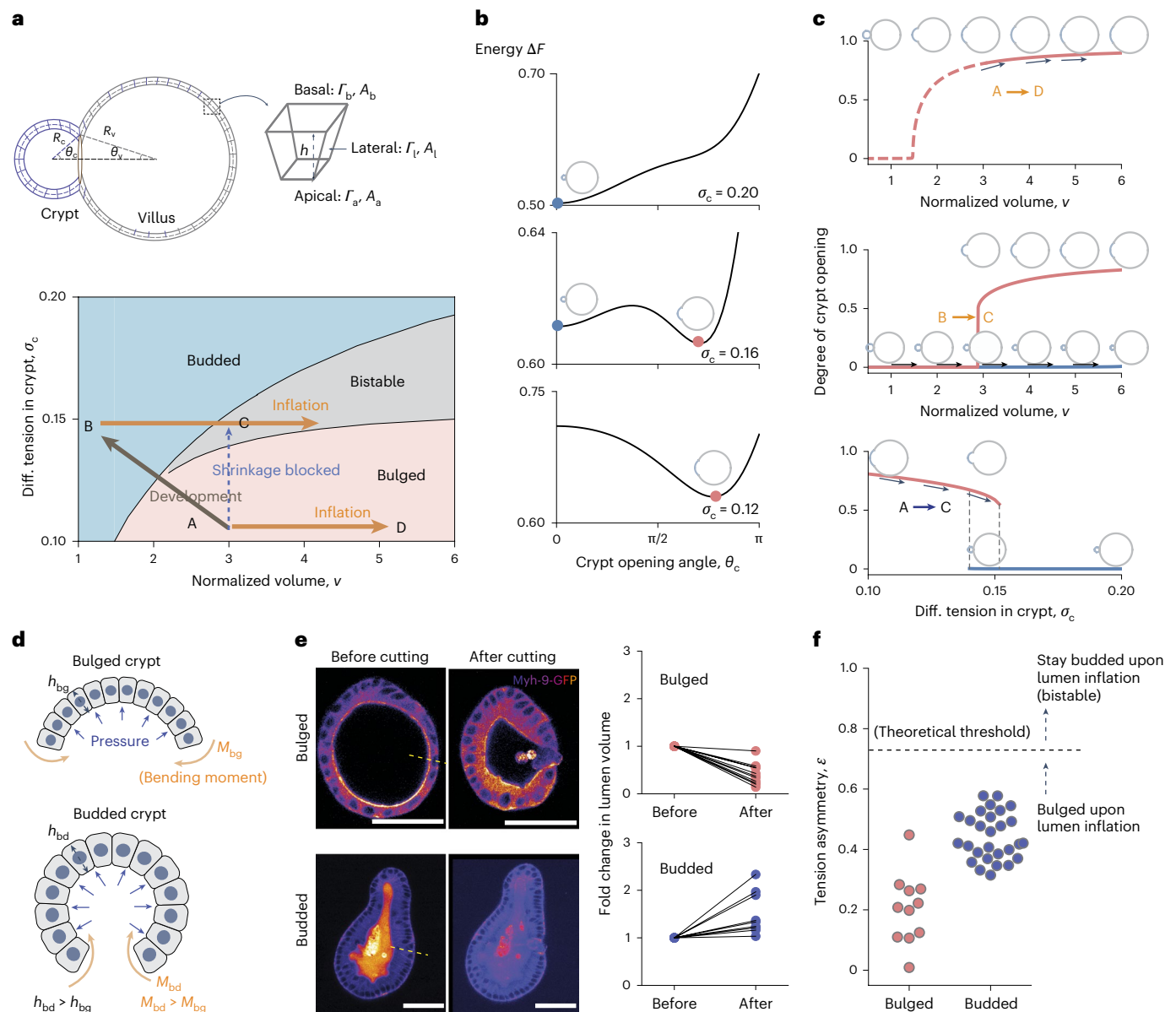


Fig. 2 | Theory of bistable crypt morphology switched by lumen volume. **a**, Schematic of a 3D vertex model (top) and the phase diagram of crypt morphology (bottom) as a function of crypt differential tension σ_c and normalized volume v . In the schematic, R_c and R_v are the radii of curvature in the crypt and villus, respectively; h is the cell height/tissue thickness (Supplementary Note 1.1). **b**, Three possible energy landscapes that control the crypt morphology ($v = 4$). Local energy minima are crypt equilibrium states, with $\theta_c = 0$ indicating the budded (or closed) crypt shape and $\theta_c > 0$ indicating the bulged (or open) shape. **c**, Evolution of crypt shape with varying lumen volumes at constant differential tension $\sigma_c = 0.1$ (top) and $\sigma_c = 0.15$ (middle), and evolution

with varying crypt differential tension at a constant volume of $v = 3$ (bottom). The arrows are different paths shown in the phase diagram in **a**. **d**, Schematic of the mechanism of curvature-thickness feedback in the crypt epithelium: epithelial bending increases its thickness h and the corresponding active bending moment $M \sim \sigma_c h$, which, in turn, facilitates crypt budding. **e**, Fold changes of lumen volume before and after villus tissue breakage, in both bulged ($N = 11$) and budded ($N = 9$) organoids. Scale bars, 50 μm . **f**, Tension asymmetry of the crypt apical versus basal surfaces in bulged ($N = 11$) and budded ($N = 28$) organoids, and the theoretical threshold (dashed line) for organoids to remain in a budded/bistable state on lumen inflation.

This suggests that the experimental system could exhibit morphological hysteresis and bistability as in the model, although this needed to be systematically tested. Before turning to a more quantitative comparison between data and theory, we proceeded to better understand the mechanical origin of bistability in the model.

Mechanical origin of morphological bistability

Our 3D vertex model of intestinal organoids is conceptually related to the classical Helfrich theory for lipid vesicles with prepatterned curvatures^{48,49,50}, except for the key difference in morphological bistability observed above. However, we reasoned that unlike lipid membranes,

epithelia have a comparatively large thickness, which changes with active tensions and deformations^{22,36,51–54}.

During crypt morphogenesis, the out-of-plane deformation driven by differences in apicobasal tension tends to increase the epithelial thickness as the crypt curvature increases,^{22,46,55,56} and the driving force ('active bending moment') M arising from differential tension is also proportional to the epithelial thickness (that is, $M \sim (\Gamma_a - \Gamma_b)h$; Fig. 2d). Therefore, the epithelial thickness and out-of-plane deformation can have positive feedback: under this geometry, the bending tends to thicken the epithelium, which, in turn, enhances M and, thus, facilitates out-of-plane deformation. This effect saturates, as thicker

tissues also have higher bending stiffness. To computationally test this hypothesis, we examined an alternative model in which the crypt thickness is kept constant, and confirmed that bistability was absent (Extended Data Fig. 4h and Supplementary Note 1.4). Overall, purely mechanical feedback can, thus, provide a potential explanation for crypt bistability and, thus, the history-dependent effects of lumen volume changes that we observed experimentally.

Next, we aimed to quantitatively test this hypothesis. We noticed that the proposed theoretical mechanism only works when the lumen of the organoid is initially swollen, that is, when the fluid pressure exerts tension on the epithelium ($\nu > 1$ in the phase diagram; Fig. 2a). We, thus, inferred the mechanical state of the lumen by experimentally measuring its volume before and after inducing epithelial breakage with 3D localized laser ablation of the tissue: if the lumen is initially swollen, tissue breakage will then let the luminal fluid flow out, and vice versa. Importantly, these measurements (Fig. 2e and Extended Data Fig. 2d) confirmed that bulged organoids are in the swollen state ($\nu \approx 2.77 \pm 1.27$, mean \pm s.d.), whereas budded samples are slightly shrunk ($\nu \approx 0.71 \pm 0.18$)—consistent with the 20–80% decrease in lumen volume observed during normal organoid morphogenesis from the bulged to budded shapes²². Furthermore, we quantitatively reanalysed osmotic deflation experiments²² in terms of the crypt opening angle, and found that a 60% lumen volume decrease is sufficient to drive fast crypt budding, which is consistent with our inferred value for ν (Extended Data Fig. 3a,b and Supplementary Note 1.3).

Importantly, however, with this experimentally inferred value of lumen volume, bistability is only predicted to occur in a very limited parameter range of tensions σ_c (0.14–0.15; Fig. 2a), which would require extreme fine tuning of cellular tensions in organoids. Given the natural variabilities in myosin and tension levels²², this scenario would fail to ensure the robustness of crypt morphogenesis. Furthermore, given previous findings that myosin intensity ratios can serve as a good proxy for tension ratios^{57,58,59}, we quantified the intensities of the fluorescent reporter for the force-generating non-muscle myosin II isoform (Myh9-GFP) in the crypt apical and basal surfaces to calculate the in-plane-to-lateral tension ratio $\frac{\Gamma_a + \Gamma_b}{\Gamma_l}$ and in-plane tension ratio α (Extended Data Figs. 7–9), as well as estimate the ‘tension asymmetry’ in the crypt apical and basal tensions, defined as $\epsilon = \frac{\Gamma_a - \Gamma_b}{\Gamma_a + \Gamma_b}$ (Supplementary Note 3 provides details on the quantifications and data-model comparisons). Importantly, we found that tension asymmetries ϵ in the budded crypts are below the theoretical threshold required for organoids to stay within the budded or bistable region of the phase diagram on lumen inflation (Fig. 2f and Supplementary Note 4.2). This discrepancy with our experimental data (Fig. 1a,e) indicates that although the model can qualitatively resolve the paradox of distinct lumen inflation effects at different time points, other mechanisms must be at play to ensure that organoids robustly remain in the bistable region of the phase diagram (rather than re-entering the ‘bulged crypt’ region) on mechanical perturbations.

Morphological bistability with mechanosensitivity of crypts

So far, we have assumed that lumen volume changes and actomyosin tensions are fully independent parameters. However, the volume and pressure of the luminal fluid have a direct impact on the geometry and stresses of the crypt tissue, which could feed back on cellular surface tension via a variety of mechanosensitive mechanisms, as described in other model systems^{60–63}. Furthermore, stem cells in crypts were found to be mechanosensitive as evidenced by the upregulation of Piezo1 and loss of stemness, on organoid inflation³⁸. Recent in vitro experiments on substrates of well-defined geometries have also revealed that intestinal crypt formation can be biased by substrate curvature^{64–66}, in line with a growing body of evidence of

mechanosensation from tissue curvature^{56,67,68}. On the basis of these findings, we considered two generic mechanisms of mechanotransduction: (1) stress-dependent feedback in which the mechanical stresses in the crypt modulates actomyosin tensions; or (2) curvature-/geometry-dependent feedback in which the curvature of the crypt cells influences actomyosin tensions. Given that both models give rise to qualitatively similar theoretical predictions (Extended Data Figs. 5 and 6 and Supplementary Note 2), we concentrate here on curvature-dependent feedback, as the curvature is easier to measure experimentally than stress (Fig. 3a; Supplementary Notes 2.2, 4.1 and 4.2 provide an alternative case). More specifically, we consider the equation $\sigma_c = \sigma \left(\frac{R_c}{R_0} \right)^{-n}$, where the crypt differential tension σ_c depends

on an intrinsic value σ (set by the stem cell fate²²) and on the crypt radius of curvature R_c (normalized by a reference value before morphogenesis R_0), with n being the coefficient quantifying the coupling strength.

Interestingly, such feedback functions distinctly in bulged versus budded crypts (Fig. 3b and Extended Data Fig. 5): decreasing the lumen volume in bulged organoids (as occurs in normal organoid development) causes an increase in the crypt differential tension, because it affects the crypt geometry. Thus, lumen deflation critically contributes to crypt morphogenesis, both by its direct mechanical impact (decreasing the monolayer tension) and indirect mechanosensitive consequence (increasing the actomyosin differential tension σ_c). However, once the differential tension is sufficiently high such that the crypt becomes budded, as previously discussed (Fig. 2a–c), the system is mechanically ‘trapped’ in the budded shape as it becomes energetically more favourable to deform the villus cells, rather than the crypt cells, on inflation.

Lumen volume changes affect actomyosin localization

To test these predictions, we first experimentally validated the key modelling assumption that differential tension is dependent on crypt geometry and lumen volume. Thus, we increased the lumen volume in early bulged or late budded organoids by treatment with prostaglandin E2 (PGE). We had previously shown that this results in crypt opening in bulged organoids, but no change in the budded crypt geometry²². Importantly, we found that these volume perturbations resulted in very different consequences on the levels and localization of myosin in bulged versus budded crypts. Although bulged crypts displayed lowered apical-to-basal myosin ratio on volume inflation in a dose-dependent manner (Fig. 3c), budded crypts did not show a consistent change (Fig. 3d). This argues that the changes in actomyosin localization in bulged crypts are not a secondary effect of osmotic changes on inflation, but are linked to changes in crypt geometry. Furthermore, inflation and myosin response occurred much faster (15–30 min; Fig. 3c,d) than the timescales of cell fate or lumen volume change during morphogenesis, justifying our quasistatic theoretical setting (Fig. 3b; Extended Data Fig. 10a–c and Supplementary Note 5 provide a full consideration of different timescales).

Importantly, across all the bulged and budded inflation data, we found a consistent trend linking the relative actomyosin intensity to crypt curvature (Fig. 3e). We then used this general relationship to quantitatively parameterize the mechanosensitive feedback between apicobasal tensions and geometry in the model (that is, $\bar{\epsilon} = \bar{R}_c^{-n}$), leading to a fit for the mechanosensitivity factor of $n = 1.0 \pm 0.5$ (Supplementary Note 4.1). On incorporation of this mechanosensitive coupling parameter, the theory predicted much broader regions of shape bistability (Extended Data Fig. 5c,d; for instance, at $\nu = 3$, bistability occurs when σ is between 0.02 and 0.04—a range that is an order of magnitude broader than without mechanosensing), which allows for a robust and irreversible budding of crypts with various intrinsic tensions. Quantitatively, mechanosensing lowered the differential tension threshold for bistability (that is, the boundary between bulged and budded

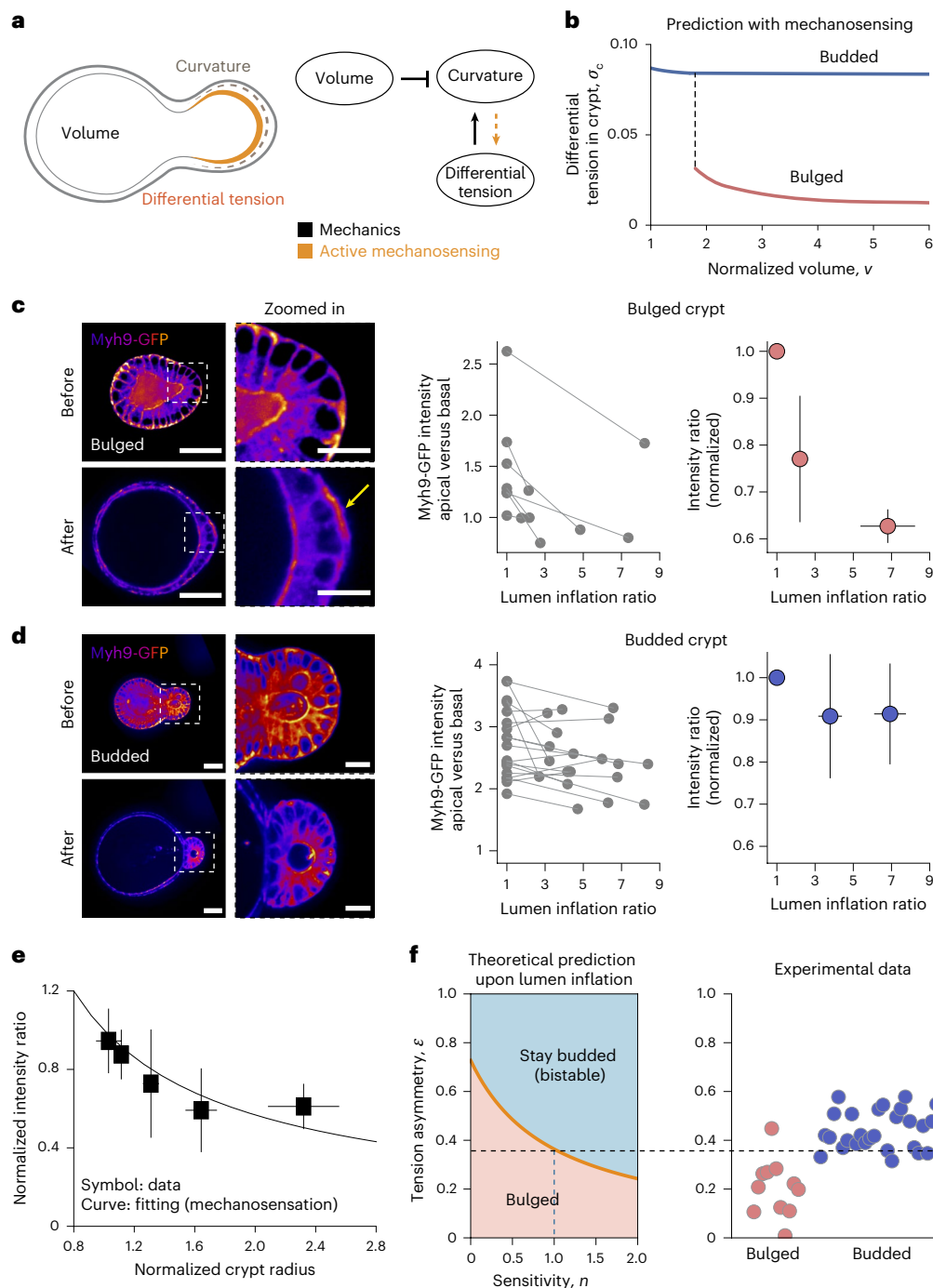


Fig. 3 | Morphological bistability with mechanosensitivity of crypts.

a, Schematic of the feedback mechanism that involves both mechanical forces and mechanosensitivity of crypt cells: lumen volume and apical-to-basal tension difference affect the curvature of the crypt due to passive force balance, whereas active mechanosensing can result in the geometry/mechanics of the crypt feedback on apical/basal tensions. **b**, Theoretical prediction of the dependence of crypt differential tension on lumen volume, in both bulged and budded organoids, when assuming mechanosensation: in bulged organoids, inflation results in crypt opening that negatively regulates tensions by mechanosensing, whereas budded organoids have structurally stable crypts that do not open on inflation that, thus, do not trigger an active response. **c,d**, Left, Myh9-GFP distribution on crypt surfaces, before and after lumen inflation (with time interval between these two states being 15–30 min). After

lumen inflation, bulged crypts show basal actomyosin relocation (yellow arrow). Right, apical-to-basal Myh9-GFP intensity ratio in bulged (**c**; $N = 7$) and budded (**d**; $N = 19$) crypt cells. Both raw data and mean values \pm s.d. of data are shown. **e**, Experimental data (symbols, presented as mean values \pm s.d.) and fitting (line) of mechanosensitivity, both apical-to-basal Myh9-GFP intensity ratio and crypt radius after lumen inflation are normalized by their values before inflation. Both bulged ($N = 24$) and budded ($N = 28$) samples are included. The fitting curve is $y = x^{-0.5}$. **f**, Influence of sensitivity factor n on the predicted threshold for organoids to remain in the budded/bistable state on lumen inflation, and comparison with experimental data of bulged ($N = 11$) and budded ($N = 28$) samples for the estimated value of $n = 1.0$ (inferred from the best-fit value in **e**; see the main text and Supplementary Note 4 for details). Scale bars, 50 μm (organoid); 20 μm (zoomed-in image).

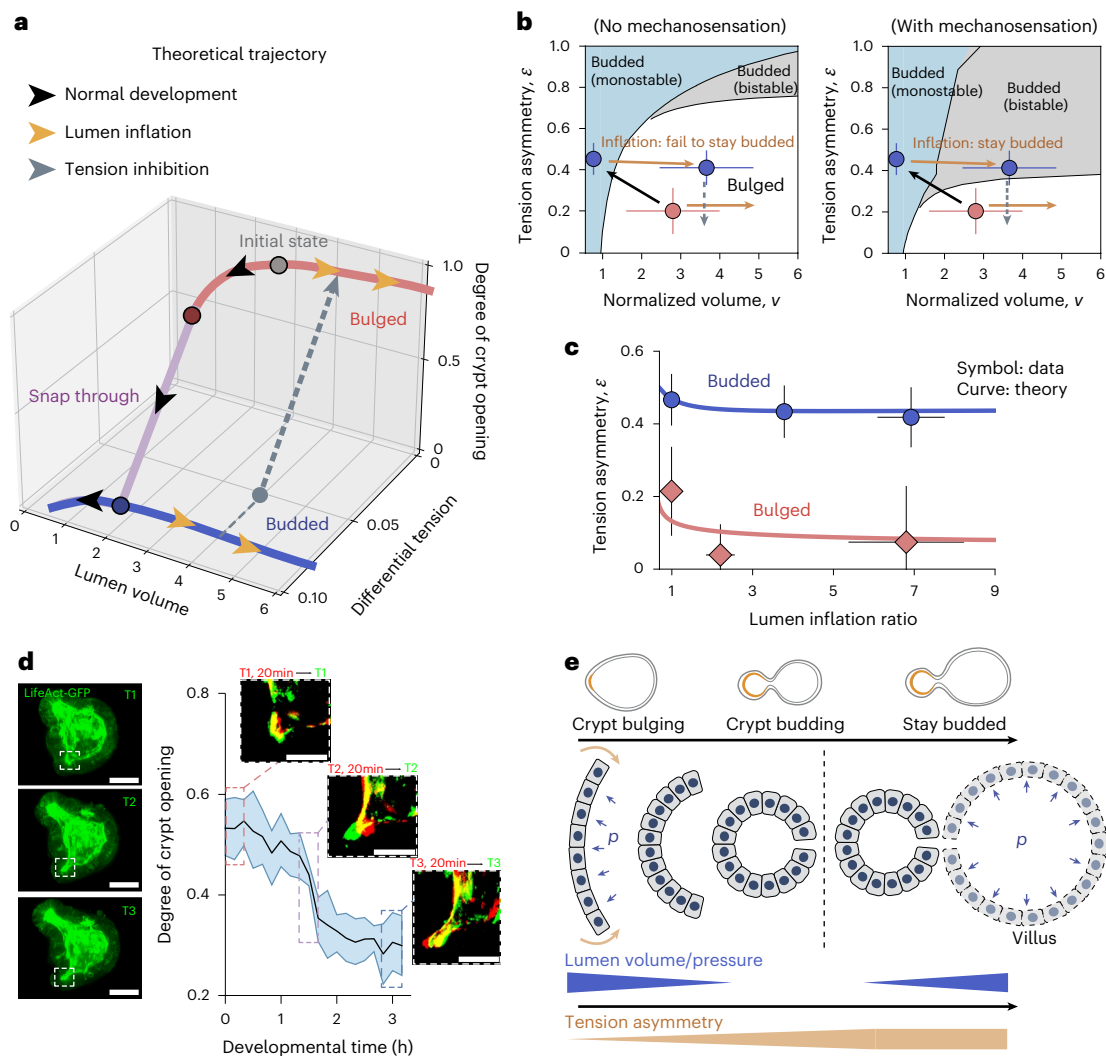


Fig. 4 | Theoretical predictions of mechanochemical bistability for crypt morphogenesis. **a**, Theoretical bifurcation trajectories showing the evolution of crypt morphology and differential tension with lumen volume, specified as normal morphogenesis (black arrows), lumen inflation of both bulged and budded organoids (orange arrows), and tension inhibition (grey arrows). **b**, Comparison between experimental data (red dot, bulged ($N = 11$) samples; blue dots, budded ($N = 28$) samples; all data presented as mean \pm s.d.) and predicted phase diagrams of crypt morphology as a function of tension asymmetry ϵ and normalized volume v . Tension asymmetry of budded organoids agrees with the prediction considering crypt mechanosensation (right) rather than that without mechanosensation (left; see also Fig. 2f). **c**, Predicted evolution for tension

asymmetry data (mean \pm s.d.) of both bulged ($N = 7$) and budded ($N = 19$) samples with the theoretical model, where the intrinsic differential tension σ is the only free parameter fitted as 0.02 (Supplementary Note 4.3). **d**, Evolution of crypt shape with developmental time ($N = 5$), showing rapid changes in shape at a critical morphological point, as expected from bistability. The solid line represents mean values and the shaded region represents 95% confidence intervals. For different developmental stages, changes in the crypt profiles in a time interval of 20 min (red, start of interval; green, end of interval) are shown. Scale bars, 50 μm . **e**, Schematic of crypt morphogenesis driven by luminal pressure, and involved morphological bistability feature arising from mechanosensation.

phases). As a key consequence, we found that the tension asymmetry ϵ , previously inferred from Myh9-GFP in budded crypts, is now above the theoretical threshold for bistability, enabling budded organoids to robustly remain budded on arbitrarily large lumen inflation (Figs. 3f and 4a,b and Supplementary Note 4.2). As an additional quantitative control, we also found that the threshold was still above the tension asymmetry ϵ from bulged crypts, supporting the experimental observation that bulged crypts require lumen volume decrease to bud (Figs. 3f and 4a,b).

Quantitative morphogenetic trajectories of organoids

To summarize these findings, we derived the predicted trajectory of organoids with mechanosensing (Fig. 4a), which can reproduce the bistable hysteresis on both crypt morphology and crypt cellular

tensions (Fig. 4b). Lumen shrinkage is critical during normal crypt morphogenesis, by both decreasing the cost associated with tissue bending (passive mechanical effect) and increasing the differential tension (active mechanosensing effect). By contrast, subsequent lumen inflation in budded organoids does not cause the system to transition back to open-crypt morphologies and crypt cellular tensions are maintained. More quantitatively, the model can simultaneously fit cell tension data from both bulged and budded samples (Fig. 4c), with the single fitting parameter (intrinsic differential tension in the crypt) of $\sigma = 0.02$ (Supplementary Note 4.3).

Second, we sought to challenge the model with further temporal pharmacological perturbations (Extended Data Fig. 3c,d). We had previously shown that impairing contractility with blebbistatin in budded crypts results in crypt opening, that is, reversal towards a monostable bulged state²². However, the model also makes the key prediction that

if we wash out blebbistatin but maintain the organoid in the swollen state, crypts should not be able to revert to budded morphologies (Fig. 4a), as the organoids go back to the bistable-parameter region from a budged state. To test this, we first treated budded organoids for 12 h with both blebbistatin and PGE, resulting in swollen organoids with bulged crypts (Extended Data Fig. 3d). We then washed out the blebbistatin, but retained the PGE. Strikingly, organoids remained swollen for around 12–24 h, and crypts did not revert to their budded morphology despite the blebbistatin washout (Extended Data Fig. 3d), consistent with the model. This provides further evidence that bistability confers history-dependent properties to crypt morphogenesis. Furthermore, after this time period, the lumen volume started decreasing in some organoids despite the presence of PGE, and we found that this was correlated to crypt budding, as that during normal organoid morphogenesis. This shows that pharmacological treatment did not have secondary effects that would cause an irreversible loss of budding ability (Extended Data Fig. 3d).

Finally, a non-trivial prediction from this model is that crypt morphologies should first vary relatively little with increasing apical tension and decreasing volume, before abruptly changing at the critical transition point. Thus, although crypt apical tension and lumen volume change gradually²², this would predict that the transition to a budded crypt should be fast as the organoid switches from one stable minimum of its energy landscape to another (snap-through bifurcation). Interestingly, plotting the crypt opening angles for different organoids as a function of time revealed a phase of abrupt closure (within 20 min; Fig. 4d), compared with a total time of around 24 h for full organoid morphogenesis (Fig. 1b and ref. 22).

Discussion

In this work, we have combined a minimal description of a 3D epithelial monolayer shape, together with mechanosensitive couplings. Although we had previously shown that different cell fates pattern different mechanical properties²², here we further show that this provides a necessary but not sufficient condition for crypt budding, as additional feedback from enterocyte-mediated lumen volume changes modulate crypt tensions via mechanosensation. We constrain this theory based on detailed morphometric measurements of cell shape in intestinal organoids as well as live reporters of myosin activity on mechanical perturbations, namely, lumen inflation. We show that a bistable region in the organoid phase space generically arises, which can explain a number of experimental features on how lumen volume changes can mediate different responses at different morphogenetic time points (Figs. 1a and 4a). Indeed, the presence of bistability confers strong hysteretic behaviour to the system, so that lumen volume changes can be a key control parameter during the regular process of organoid morphogenesis as well as be rendered irrelevant once budded crypt morphogenesis is completed (Fig. 4e). This bears conceptual similarities to the role of prepatterned versus self-organized/self-reinforcing cues in other developmental systems, such as the mechanochemical interplay of embryo polarization in *Caenorhabditis elegans*^{69,70}. This might, therefore, be a general mechanism that could ensure the robustness and irreversibility of morphogenesis in multicellular systems. The next important step would be to understand the molecular mechanosensing mechanisms that mediate the feedback from crypt morphology to actomyosin localization. Our inflation and deflation data suggest that this feedback is relatively fast (15–30 min) and reversible, although further work could also dissect whether additional feedback can occur on longer timescales of days, for instance, via cell fate maturation.

Our work also provides an example of the emerging role of fluid lumen pressure in controlling morphogenesis^{11,14,17,19}. Compared with other types of biological force, fluid pressure has the advantage of being intrinsically long ranged. For instance, in intestinal morphogenesis, an outstanding question that remains is the nature of coordination between the specification and maturation of different crypts,

both in vivo and in vitro. In organoids, lumen volume changes would be expected to provide a global cue that is felt equally among all the crypts of an organoid regardless of its size. Coupled with mechanosensing, this mechanism could allow for the synchronization of crypt morphogenesis, especially as the earlier crypt fate specification events are rather asynchronous³⁷. Given that crypt fission was also shown to be dependent on lumen volume changes³⁸, such mechanism could also act at multiple different time points during development. Importantly, even without fluid pressure, in vivo crypts can still be subjected to other external forces, arising, for instance, from the constriction of the smooth muscle layers⁹ or from the osmotic swelling of villus cells²². To test whether our proposed mechanism might also apply to geometries closed to the in vivo situation within an open tube, we performed additional theoretical analyses, in which crypts are under apical constriction and experience external forces directly from the surrounding villus tissue. Interestingly, we found a phase diagram very similar to the case of 3D organoids, showing that our mechanochemical bistability mechanism does not rely on a closed lumen, but generically arises in the presence of out-of-plane bending forces in the crypt combined with in-plane forces exerted by villus cells (Extended Data Fig. 10d,e and Supplementary Note 6). In the future, it will be important to understand—at the cellular and molecular levels—the mechanisms of the relationship between osmotic forces, lumen volume, crypt geometry and actomyosin accumulation, as well as to test whether similar principles of bistability and robustness of morphogenesis hold in other developmental and organoid systems.

Online content

Any methods, additional references, Nature Portfolio reporting summaries, source data, extended data, supplementary information, acknowledgements, peer review information; details of author contributions and competing interests; and statements of data and code availability are available at <https://doi.org/10.1038/s41567-025-02792-1>.

References

- Collinet, C. & Lecuit, T. Programmed and self-organized flow of information during morphogenesis. *Nat. Rev. Mol. Cell Biol.* **22**, 245–265 (2021).
- Goodwin, K. & Nelson, C. M. Mechanics of development. *Dev. Cell* **56**, 240–250 (2021).
- Heisenberg, C. P. & Bellaïche, Y. Forces in tissue morphogenesis and patterning. *Cell* **153**, 948–962 (2013).
- Lecuit, T. & Lenne, P. F. Cell surface mechanics and the control of cell shape, tissue patterns and morphogenesis. *Nat. Rev. Mol. Cell Biol.* **8**, 633–644 (2007).
- Hannezo, E., Prost, J. & Joanny, J. F. Instabilities of monolayered epithelia: shape and structure of villi and crypts. *Phys. Rev. Lett.* **107**, 078104 (2011).
- Karzbrun, E. et al. Human brain organoids on a chip reveal the physics of folding. *Nat. Phys.* **14**, 515–522 (2018).
- Li, B., Cao, Y. P., Feng, X. Q. & Gao, H. Surface wrinkling of mucosa induced by volumetric growth: theory, simulation and experiment. *J. Mech. Phys. Solids* **59**, 758–774 (2011).
- Savin, T. et al. On the growth and form of the gut. *Nature* **476**, 57–62 (2011).
- Shyer, A. E. et al. Villification: how the gut gets its villi. *Science* **342**, 212–218 (2013).
- Trushko, A. et al. Buckling of an epithelium growing under spherical confinement. *Dev. Cell* **54**, 655–668 (2020).
- Chan, C. J. et al. Hydraulic control of mammalian embryo size and cell fate. *Nature* **571**, 112–116 (2019).
- Chartier, N. T. et al. A hydraulic instability drives the cell death decision in the nematode germline. *Nat. Phys.* **17**, 920–925 (2021).
- Dasgupta, S., Gupta, K., Zhang, Y., Viasnoff, V. & Prost, J. Physics of lumen growth. *Proc. Natl Acad. Sci. USA* **115**, E4751–E4757 (2018).

14. Dumortier, J. G. et al. Hydraulic fracturing and active coarsening position the lumen of the mouse blastocyst. *Science* **365**, 465–468 (2019).
15. Huljev, K. et al. A hydraulic feedback loop between mesendoderm cell migration and interstitial fluid relocalization promotes embryonic axis formation in zebrafish. *Dev. Cell* **58**, 582–596 (2023).
16. Le Verge-Serandour, M. & Turlier, H. A hydro-osmotic coarsening theory of biological cavity formation. *PLoS Comput. Biol.* **17**, e1009333 (2021).
17. Munjal, A., Hannezo, E., Tsai, T. Y. C., Mitchison, T. J. & Megason, S. G. Extracellular hyaluronate pressure shaped by cellular tethers drives tissue morphogenesis. *Cell* **184**, 6313–6325 (2021).
18. Nelson, C. M. et al. Microfluidic chest cavities reveal that transmural pressure controls the rate of lung development. *Development* **144**, 4328–4335 (2017).
19. Saïas, L. et al. Decrease in cell volume generates contractile forces driving dorsal closure. *Dev. Cell* **33**, 611–621 (2015).
20. Schliffka, M. F., Dumortier, J. G., Pelzer, D., Mukherjee, A. & Maître, J. L. Inverse blebs operate as hydraulic pumps during mouse blastocyst formation. *Nat. Cell Biol.* **26**, 1669–1677 (2024).
21. Stokkermans, A. et al. Muscular hydraulics drive larva–polyp morphogenesis. *Curr. Biol.* **32**, 4707–4718 (2022).
22. Yang, Q. et al. Cell fate coordinates mechano-osmotic forces in intestinal crypt formation. *Nat. Cell Biol.* **23**, 733–744 (2021).
23. Hannezo, E. & Heisenberg, C. P. Mechanochemical feedback loops in development and disease. *Cell* **178**, 12–25 (2019).
24. Pinheiro, D., Kardos, R., Hannezo, É. & Heisenberg, C. P. Morphogen gradient orchestrates pattern-preserving tissue morphogenesis via motility-driven unjamming. *Nat. Phys.* **18**, 1482–1493 (2022).
25. Valet, M., Siggia, E. D. & Brivanlou, A. H. Mechanical regulation of early vertebrate embryogenesis. *Nat. Rev. Mol. Cell Biol.* **23**, 169–184 (2022).
26. Zinner, M., Lukonin, I. & Liberali, P. Design principles of tissue organisation: how single cells coordinate across scales. *Curr. Opin. Cell Biol.* **67**, 37–45 (2020).
27. Erzberger, A., Jacobo, A., Dasgupta, A. & Hudspeth, A. J. Mechanochemical symmetry breaking during morphogenesis of lateral-line sensory organs. *Nat. Phys.* **16**, 949–957 (2020).
28. Fabrèges, D. et al. Temporal variability and cell mechanics control robustness in mammalian embryogenesis. *Science* **386**, eadh1145 (2024).
29. Guo, H., Swan, M. & He, B. Optogenetic inhibition of actomyosin reveals mechanical bistability of the mesoderm epithelium during *Drosophila* mesoderm invagination. *eLife* **11**, e69082 (2022).
30. Haas, P. A., Höhn, S. S., Honerkamp-Smith, A. R., Kirkegaard, J. B. & Goldstein, R. E. The noisy basis of morphogenesis: mechanisms and mechanics of cell sheet folding inferred from developmental variability. *PLoS Biol.* **16**, e2005536 (2018).
31. Menshykau, D., Blanc, P., Unal, E., Sapin, V. & Iber, D. An interplay of geometry and signaling enables robust lung branching morphogenesis. *Development* **141**, 4526–4536 (2014).
32. Niwayama, R. et al. A tug-of-war between cell shape and polarity controls division orientation to ensure robust patterning in the mouse blastocyst. *Dev. Cell* **51**, 564–574 (2019).
33. Staddon, M. F., Cavanaugh, K. E., Munro, E. M., Gardel, M. L. & Banerjee, S. Mechanosensitive junction remodeling promotes robust epithelial morphogenesis. *Biophys. J.* **117**, 1739–1750 (2019).
34. Tsai, T. Y. C. et al. An adhesion code ensures robust pattern formation during tissue morphogenesis. *Science* **370**, 113–116 (2020).
35. Sumigra, K. D., Terwilliger, M. & Lechler, T. Morphogenesis and compartmentalization of the intestinal crypt. *Dev. Cell* **45**, 183–197 (2018).
36. Pérez-González, C. et al. Mechanical compartmentalization of the intestinal organoid enables crypt folding and collective cell migration. *Nat. Cell Biol.* **23**, 745–757 (2021).
37. Serra, D. et al. Self-organization and symmetry breaking in intestinal organoid development. *Nature* **569**, 66–72 (2019).
38. Tallapragada, N. P. et al. Inflation-collapse dynamics drive patterning and morphogenesis in intestinal organoids. *Cell Stem Cell* **28**, 1516–1532.e14 (2021).
39. Sato, T. et al. Single Lgr5 stem cells build crypt-villus structures in vitro without a mesenchymal niche. *Nature* **459**, 262–265 (2009).
40. Hartl, L., Huelsh-Prince, G., van Zon, J. & Tans, S. J. Apical constriction is necessary for crypt formation in small intestinal organoids. *Dev. Biol.* **450**, 76–81 (2019).
41. Alon, U. Network motifs: theory and experimental approaches. *Nat. Rev. Genet.* **8**, 450–461 (2007).
42. Zhao, J., Perkins, M. L., Norstad, M. & Garcia, H. G. A bistable autoregulatory module in the developing embryo commits cells to binary expression fates. *Curr. Biol.* **33**, 2851–2864 (2023).
43. Alt, S., Ganguly, P. & Salbreux, G. Vertex models: from cell mechanics to tissue morphogenesis. *Philos. Trans. R. Soc. B* **372**, 20150520 (2017).
44. Fletcher, A. G., Osterfield, M., Baker, R. E. & Shvartsman, S. Y. Vertex models of epithelial morphogenesis. *Biophys. J.* **106**, 2291–2304 (2014).
45. Hannezo, E., Prost, J. & Joanny, J. F. Theory of epithelial sheet morphology in three dimensions. *Proc. Natl Acad. Sci. USA* **111**, 27–32 (2014).
46. Rozman, J., Krajnc, M. & Zihler, P. Collective cell mechanics of epithelial shells with organoid-like morphologies. *Nat. Commun.* **11**, 3805 (2020).
47. Turlier, H., Audoly, B., Prost, J. & Joanny, J. F. Furrow constriction in animal cell cytokinesis. *Biophys. J.* **106**, 114–123 (2014).
48. Döbereiner, H. G. & Seifert, U. Giant vesicles at the prolate-oblate transition: a macroscopic bistable system. *Europhys. Lett.* **36**, 325 (1996).
49. Jülicher, F. & Lipowsky, R. Shape transformations of vesicles with intramembrane domains. *Phys. Rev. E* **53**, 2670–2683 (1996).
50. Zimmerberg, J. & Kozlov, M. M. How proteins produce cellular membrane curvature. *Nat. Rev. Mol. Cell Biol.* **7**, 9–19 (2006).
51. Iber, D. & Vetter, R. 3D organisation of cells in pseudostratified epithelia. *Front. Phys.* **10**, 898160 (2022).
52. Khoromskaia, D. & Salbreux, G. Active morphogenesis of patterned epithelial shells. *eLife* **12**, e75878 (2023).
53. Messal, H. A. et al. Tissue curvature and apicobasal mechanical tension imbalance instruct cancer morphogenesis. *Nature* **566**, 126–130 (2019).
54. Recho, P. et al. Tug-of-war between stretching and bending in living cell sheets. *Phys. Rev. E* **102**, 012401 (2020).
55. Krajnc, M. & Zihler, P. Theory of epithelial elasticity. *Phys. Rev. E* **92**, 052713 (2015).
56. Luciano, M. et al. Cell monolayers sense curvature by exploiting active mechanics and nuclear mechanoadaptation. *Nat. Phys.* **17**, 1382–1390 (2021).
57. Salbreux, G., Charras, G. & Paluch, E. Actin cortex mechanics and cellular morphogenesis. *Trends Cell Biol.* **22**, 536–545 (2012).
58. Chugh, P. & Paluch, E. K. The actin cortex at a glance. *J. Cell Sci.* **131**, jcs186254 (2018).
59. Streichan, S. J., Lefebvre, M. F., Noll, N., Wieschaus, E. F. & Shraiman, B. I. Global morphogenetic flow is accurately predicted by the spatial distribution of myosin motors. *eLife* **7**, e27454 (2018).
60. Desprat, N., Supatto, W., Pouille, P. A., Beaurepaire, E. & Farge, E. Tissue deformation modulates twist expression to determine anterior midgut differentiation in *Drosophila* embryos. *Dev. Cell* **15**, 470–477 (2008).

61. Fernandez-Gonzalez, R., de Matos Simoes, S., Röper, J. C., Eaton, S. & Zallen, J. A. Myosin II dynamics are regulated by tension in intercalating cells. *Dev. Cell* **17**, 736–743 (2009).
 62. Okuda, S. et al. Strain-triggered mechanical feedback in self-organizing optic-cup morphogenesis. *Sci. Adv.* **4**, eaau1354 (2018).
 63. Pouille, P. A., Ahmadi, P., Brunet, A. C. & Farge, E. Mechanical signals trigger myosin II redistribution and mesoderm invagination in *Drosophila* embryos. *Sci. Signal.* **2**, ra16 (2009).
 64. Gjorevski, N. et al. Tissue geometry drives deterministic organoid patterning. *Science* **375**, eaaw9021 (2022).
 65. Nikolaev, M. et al. Homeostatic mini-intestines through scaffold-guided organoid morphogenesis. *Nature* **585**, 574–578 (2020).
 66. Pentimikko, N. et al. Cellular shape reinforces niche to stem cell signaling in the small intestine. *Sci. Adv.* **8**, eabm1847 (2022).
 67. Mobasser, S. A. et al. Patterning of human epidermal stem cells on undulating elastomer substrates reflects differences in cell stiffness. *Acta Biomater.* **87**, 256–264 (2019).
 68. Tomba, C., Luchnikov, V., Barberi, L., Blanch-Mercader, C. & Roux, A. Epithelial cells adapt to curvature induction via transient active osmotic swelling. *Dev. Cell* **57**, 1257–1270.e5 (2022).
 69. Gross, P. et al. Guiding self-organized pattern formation in cell polarity establishment. *Nat. Phys.* **15**, 293–300 (2019).
 70. Sailer, A., Anneken, A., Li, Y., Lee, S. & Munro, E. Dynamic opposition of clustered proteins stabilizes cortical polarity in the *C. elegans* zygote. *Dev. Cell* **35**, 131–142 (2015).
- Publisher's note** Springer Nature remains neutral with regard to jurisdictional claims in published maps and institutional affiliations.
- Open Access** This article is licensed under a Creative Commons Attribution 4.0 International License, which permits use, sharing, adaptation, distribution and reproduction in any medium or format, as long as you give appropriate credit to the original author(s) and the source, provide a link to the Creative Commons licence, and indicate if changes were made. The images or other third party material in this article are included in the article's Creative Commons licence, unless indicated otherwise in a credit line to the material. If material is not included in the article's Creative Commons licence and your intended use is not permitted by statutory regulation or exceeds the permitted use, you will need to obtain permission directly from the copyright holder. To view a copy of this licence, visit <http://creativecommons.org/licenses/by/4.0/>.
- © The Author(s) 2025

Methods

Animal work

All the animal experiments were approved by the Basel Cantonal Veterinary Authorities and conducted in accordance with the Guide for the Care and Use of Laboratory Animals. Male and female outbred mice from 7 weeks old onwards were used for generating organoid lines of wild-type C57BL/6 and Lgr5-DTR-EGFP as reported previously²². One male mouse at 10 weeks was used to generate the organoid line of LifeAct-GFP. One male mouse at 10 weeks was used to generate the organoid line of Myh9-GFP.

Mouse lines used: wild-type C57BL/6 (Charles River Laboratories), Lgr5-DTR-EGFP (de Sauvage's laboratory, Genentech), LifeAct-GFP (T. Hiiragi's laboratory, EMBL) and Myh9-GFP (Lennon-Duménil's laboratory, Institut Curie).

Mice were kept in housing conditions with 12 h light/12 h dark cycle, 18–23 °C ambient temperature and 40–60% humidity.

Organoid culture

Organoids were generated from isolated crypts of the murine small intestine as previously described²². Organoids were kept in IntestiCult Organoid Growth Medium (STEMCELL Technologies) with 100 µg ml⁻¹ penicillin–streptomycin for amplification and maintenance.

Time-course experiments of fixed organoid samples

The method was adapted as described before²². Organoids were collected 5–7 days after passaging and digested with TrypLE (Thermo Fisher Scientific) for 20 min at 37 °C. Dissociated cells were passed through a cell strainer with a pore size of 30 µm (Sysmex). The collected cells were mixed with Matrigel (Corning) in an ENR medium to Matrigel ratio of 1:1(15). In each well of a 96-well plate, 5 µl droplets with 2,500 cells were seeded. After 15 min of solidification at 37 °C, 100 µl of the medium was overlaid. From day 0 to day 1, ENR was supplemented with 25% Wnt3a-conditioned medium (Wnt3a-CM), 10 µM Y-27632 (ROCK inhibitor, STEMCELL Technologies) and 3 µM of CHIR99021 (GSK3B inhibitor, STEMCELL Technologies, cat. no. 72054). From day 1 to day 3, ENR was supplemented with 25% Wnt3a-CM and 10 µM Y-27632. From day 3 to day 5, only ENR was added to the cells. Wnt3a-CM was produced in-house by Wnt3a L-cells (kind gift from Novartis).

Compound treatments

Compound treatments were tested in a dilution series of various concentrations from 1 mM to 5 nM as that in a previous study²².

Single cells derived from LifeAct-GFP organoids were plated in a 96-well plate chamber and exposed to 0.5 µM PGE (kind gift from Novartis) or 0.5 µM dimethyl sulfoxide (Sigma-Aldrich, cat. no. D8418) diluted in an ENR medium, from 72 h for 24 h (dimethyl sulfoxide; Fig. 1b), from 96 h for 2 h (PGE, Fig. 1d) or from 72 h for 10 h (PGE; Fig. 1c).

Single cells derived from Myh9-GFP organoids were plated in an ibidi µ-Slide eight-plate chamber and cultured in a time-course medium till 84 h or 96 h for laser nanosurgery (Fig. 2e) or PGE treatment (Fig. 3c,d).

Single cells derived from Lgr5-DTR-GFP organoids were plated in a 96-well plate chamber and cultured in a time-course medium until fixation at 72 h, 84 h or 96 h (Extended Data Fig. 1a–e).

Single cells derived from organoids wild-type C57BL/6 were plated in a 96-well plate and treated with 0.5 µM PGE (kind gift from Novartis) or 0.5 µM dimethyl sulfoxide in an ENR medium, from 72 h until fixation at 74 h, 84 h or 96 h, or from 96 h until fixation at 98 h (Fig. 1e).

Organoid immunostaining and imaging

The method was adapted from that described before²². Primary and secondary antibodies were diluted in a blocking buffer and applied. Cell nuclei were stained with 20 µg ml⁻¹ DAPI (4',6-diamidino-2-phenylindole, Invitrogen) in phosphate-buffered saline for 5 min at room temperature. Cells were stained with 1 µg ml⁻¹ of Alexa Fluor 647

carboxylic acid succinimidyl ester (CellTrace, Invitrogen) in a carbonate buffer (1.95 ml of 0.5 M NaHCO₃, 50 µl of 0.5 M Na₂CO₃, both from Sigma-Aldrich, in 8 ml of water for creating 10 ml of buffer).

High-throughput imaging was done with an automated spinning-disc microscope from Yokogawa (Cell Voyager 7000S), with an enhanced CSU-W1 spinning disc (microlens-enhanced dual Nipkow-disc confocal scanner), a ×40 (numerical aperture, 0.95) Olympus objective and a Neo scientific complementary metal–oxide–semiconductor camera (Andor, 2,560 × 2,160 pixels). For imaging, an intelligent imaging approach was used in the Yokogawa CV7000 (Search First module of Wako software 1.0) as described before²². Also, z planes spanning a range up to 90 µm and 2 or 3 µm z steps were acquired.

Confocal imaging of the fixed samples was performed using a Nikon Ti2-E Eclipse inverted microscope with a motorized stand along with a Yokogawa CSU-W1 dual camera (CAM1 SN: X-11424; CAM2 SN: 11736) T2 spinning-disc confocal scanning unit, CFIP-Fluor ×40 oil/1.4 objective and VisiView 4.4.0.9 software. Laser lines used are Toptica iBeam Smart 405/488/639 nm and Cobolt Jive 561 nm. Laser power and digital gain settings were unchanged within a given session to permit a direct comparison of expression levels among organoids stained in the same experiment. Image stacks were acquired with a slice thickness of 2 µm or less.

Confocal imaging of live Myh9-GFP samples for two time points before and after PGE inflation was performed using the same microscope and imaging settings as those used in the confocal imaging of the fixed samples. Before PGE treatment, one to five organoids from one well were quickly imaged within 10 min. Then, PGE was added into the culture medium of the same well and put back to 37 °C tissue culture. After 20–30 min, organoid lumens are sufficiently inflated. Imaging was done from the same organoids for the time point after inflation.

Time-course image analysis

Organoid segmentation in the maximum intensity projections (MIPs) was adapted from another work²². For each acquired confocal z-stack field, MIPs were generated. All the MIP fields of a well were stitched together to obtain the MIP-well overviews for each channel. The high-resolution well overviews were used for organoid segmentation and feature extraction. From the segmented MIPs, we measure and calculate the features of each individual organoid.

Light-sheet microscopy

Light-sheet microscopy was conducted using LS1 Live light-sheet microscope system (Viventis) or a similar customized microscope system as described before²². Sample mounting was performed as described previously²². For organoid imaging, LifeAct-GFP organoids were collected and digested with TrypLE (Thermo Fisher Scientific) for 20 min at 37 °C. GFP-positive cells were sorted by fluorescence-activated cell sorting and collected in a medium containing advanced DMEM/F-12 with 15 mM HEPES (STEMCELL Technologies) supplemented with 100 µg ml⁻¹ penicillin–streptomycin, 1× GlutaMAX (Thermo Fisher Scientific), 1× B-27 (Thermo Fisher Scientific), 1× N-2 (Thermo Fisher Scientific), 1 mM N-acetylcysteine (Sigma), 500 ng ml⁻¹ R-Spondin (kind gift from Novartis), 100 ng ml⁻¹ Noggin (PeproTech) and 100 ng ml⁻¹ murine EGF (R&D Systems). 2,000 cells were then embedded in a 5 µl drop of Matrigel/medium in a 50/50 ratio. Drops were placed in the imaging chamber and incubated for 20 min before being covered with 1 ml of the medium. For the first 3 days, the medium was supplemented with 20% Wnt3a-CM and 10 µM Y-27632 (ROCK inhibitor, STEMCELL Technologies). For the first day, in addition, 3 µM of CHIR99021 (STEMCELL Technologies) was supplemented. After more than 2 days of culturing in a cell culture incubator, the imaging chamber was transferred to the microscope kept at 37 °C and 5% CO₂. Different organoids were selected as the starting positions and imaged every 10 min. A volume of 150–200 µm was acquired with a z spacing of 2 µm between slices. The medium was exchanged manually under the microscopy every half-day.

Data analysis

Tissue opening angles θ_i (Fig. 2a shows the schematic, with $i = c, v$ representing the crypt and villus tissues, respectively), which is related to the degree of crypt opening (defined as $\theta_c/(\pi - \theta_v)$), can be inferred from the coordinate information of the characteristic points along the midplane of the tissue, by approximating the tissue as a spherical cap. For each region (crypt or villus) in each sample, three points are extracted from the organoid image by using the multipoint tool of Fiji (version 2.9.0)⁷¹: two at the boundary (crypt/villus), denoted as (x_1, y_1) and (x_3, y_3) , and one in the middle, denoted as (x_2, y_2) (Extended Data Fig. 2a shows the schematic). The opening angle can be calculated as

$$\theta = \pi - \arccos \frac{(x_1 - x)(x_2 - x) + (y_1 - y)(y_2 - y)}{\sqrt{[(x_1 - x)^2 + (y_1 - y)^2] \times [(x_2 - x)^2 + (y_2 - y)^2]}}$$

which involves the coordinate of the centre of the spherical tissue: $x = \frac{B}{2A}$, $y = -\frac{C}{2A}$, $A = x_1(y_2 - y_3) + x_2(y_3 - y_1) + x_3(y_1 - y_2)$, $B = (x_1^2 + y_1^2)(y_2 - y_3) + (x_2^2 + y_2^2)(y_3 - y_1) + (x_3^2 + y_3^2)(y_1 - y_2)$ and $C = (x_1^2 + y_1^2)(x_2 - x_3) + (x_2^2 + y_2^2)(x_3 - x_1) + (x_3^2 + y_3^2)(x_1 - x_2)$.

Morphometric parameters, including cell height h_i , cell width d_i and tissue radius R_i , were extracted from the images of intestinal organoids by using Fiji. Cell height (that is, epithelial thickness) h_i and cell width d_i of each region (crypt or villus) were measured by the line tool of Fiji in at least three random positions and determined as the average value of these measurements. Tissue radius R_i is defined as the average value of the apical and basal radii (Supplementary Note 1.1), and was quantified by the oval tool of Fiji.

Myh9-GFP intensity ratios in single cells were measured using Fiji (version 2.9.0) as described before²².

Lumen volume calculation of the light-sheet data was proceeded as done previously²².

Lumen breakage by laser nanosurgery

The method was adapted from previous studies²². In brief, images are captured using an LSM710 scanning confocal microscope using the ZEN Black software (the only version). The microscope is equipped with an incubation chamber to maintain the sample at 37 °C and to provide 5% CO₂. Organoids were embedded in Matrigel and cultured in ibidi eight-well plates. Cutting was performed using a wavelength of 850 nm with a Chameleon Ultra laser. All the cuttings were performed in the villus region of the organoid. The cutting region (Fig. 2e, yellow dashed lines) was set as a rectangle of 0.9 μm × 50 μm, and the activation time was calculated by the scan speed of 1.25 ms pixel⁻¹. Organoids were imaged with a Plan-Neofluar ×40/0.9 Imm Corr Ph3 objective lens before and after cutting.

Statistics and reproducibility

All the statistical analysis was performed using the Python library SciPy. All the box-plot elements show 25% (Q1, lower bounds), 50% (median, black lines within the boxes) and 75% (Q3, upper bounds) quartiles, and whiskers denote 1.5 times the interquartile range (maxima, Q3 + 1.5 × (Q3 - Q1); minima, Q1 - 1.5 × (Q3 - Q1)) with outliers (rhombuses). In compound time-course experiments, we assumed that a minimum of around 50 organoids on day 4 would be sufficient to recognize differences between control and perturbations based on historical experiments. The sample size was determined based on previous related studies in the field^{37,72–74}.

Reporting summary

Further information on research design is available in the Nature Portfolio Reporting Summary linked to this article.

Data availability

Source data are provided with this paper.

Code availability

Codes used in the current study are from previous work²² and available on https://github.com/fmi-basel/glib-nature_cell_biology2021-materials.git.

References

- Schindelin, J. et al. Fiji: an open-source platform for biological-image analysis. *Nat. Methods* **9**, 676–682 (2012).
- Fouchard, J. et al. Curling of epithelial monolayers reveals coupling between active bending and tissue tension. *Proc. Natl Acad. Sci. USA* **117**, 9377–9383 (2020).
- Lee, J. H., Park, H. S. & Holmes, D. P. Elastic instabilities govern the morphogenesis of the optic cup. *Phys. Rev. Lett.* **127**, 138102 (2021).
- Polyakov, O. et al. Passive mechanical forces control cell-shape change during *Drosophila* ventral furrow formation. *Biophys. J.* **107**, 998–1010 (2014).

Acknowledgements

We thank all members of the Hannezo and Liberali groups for fruitful discussions, as well as C. Schwayer, G. Quintas, L. Capolupo, D. Bruckner and D. Pinheiro for reading the manuscript. We also thank Y. Wu and X. Wu from the Yang group for performing experiments in the last rounds of revision and the So group at the National Institute of Biological Sciences, Beijing, for helping with the light-sheet time-lapse experiments. This work received funding from the European Research Council (ERC) under the European Union's Horizon 2020 research and innovation programme via grant agreement no. 758617 (to P.L.), Swiss National Foundation (SNF) (no. POOP3_157531 to P.L.), the ERC under the European Union's Horizon 2020 research and innovation programme under grant agreement no. 851288 (to E.H.) and the Austrian Science Fund (FWF) (no. P 31639 to E.H.). This work was supported by the National Natural Science Foundation of China via grant no.3247060387 (to Q.Y.) and the Strategic Priority Research Program of the Chinese Academy of Sciences (no. XDB0820000 to Q.Y.).

Author contributions

E.H., S.-L.X., Q.Y. and P.L. conceived the project and designed the experiments. Q.Y. performed the experiments. Q.Y. and S.-L.X. analysed the experimental data. S.-L.X. designed the physical model and performed the simulations. S.-L.X. wrote the first version of the manuscript. E.H., S.-L.X., Q.Y. and P.L. reviewed and wrote the manuscript.

Funding

Open access funding provided by Institute of Science and Technology (IST Austria).

Competing interests

The authors declare no competing interests.

Additional information

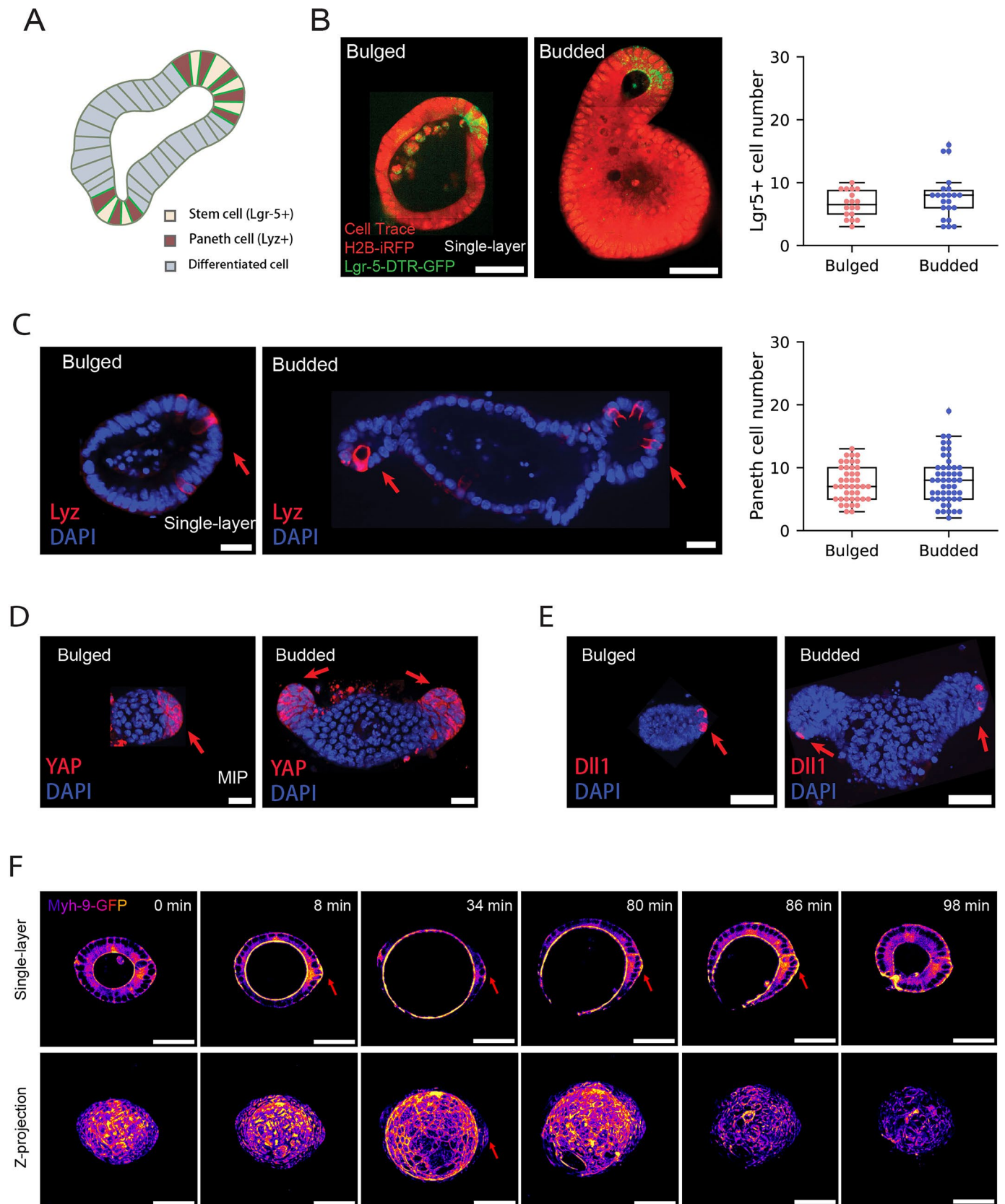
Extended data is available for this paper at <https://doi.org/10.1038/s41567-025-02792-1>.

Supplementary information The online version contains supplementary material available at <https://doi.org/10.1038/s41567-025-02792-1>.

Correspondence and requests for materials should be addressed to Prisca Liberali or Edouard Hannezo.

Peer review information *Nature Physics* thanks Zev Gartner, Vasudha Srivastava and the other, anonymous, reviewer(s) for their contribution to the peer review of this work.

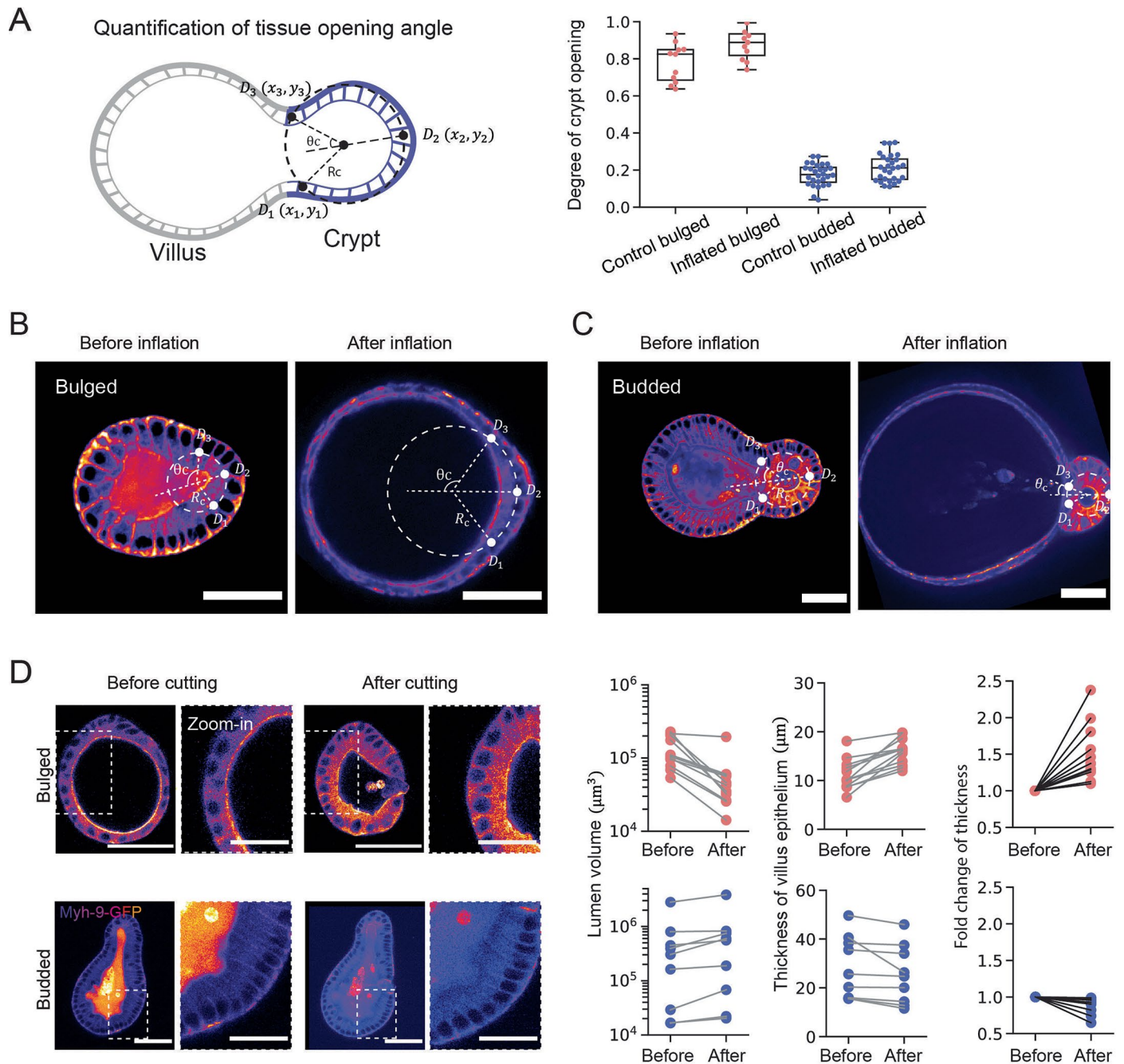
Reprints and permissions information is available at www.nature.com/reprints.

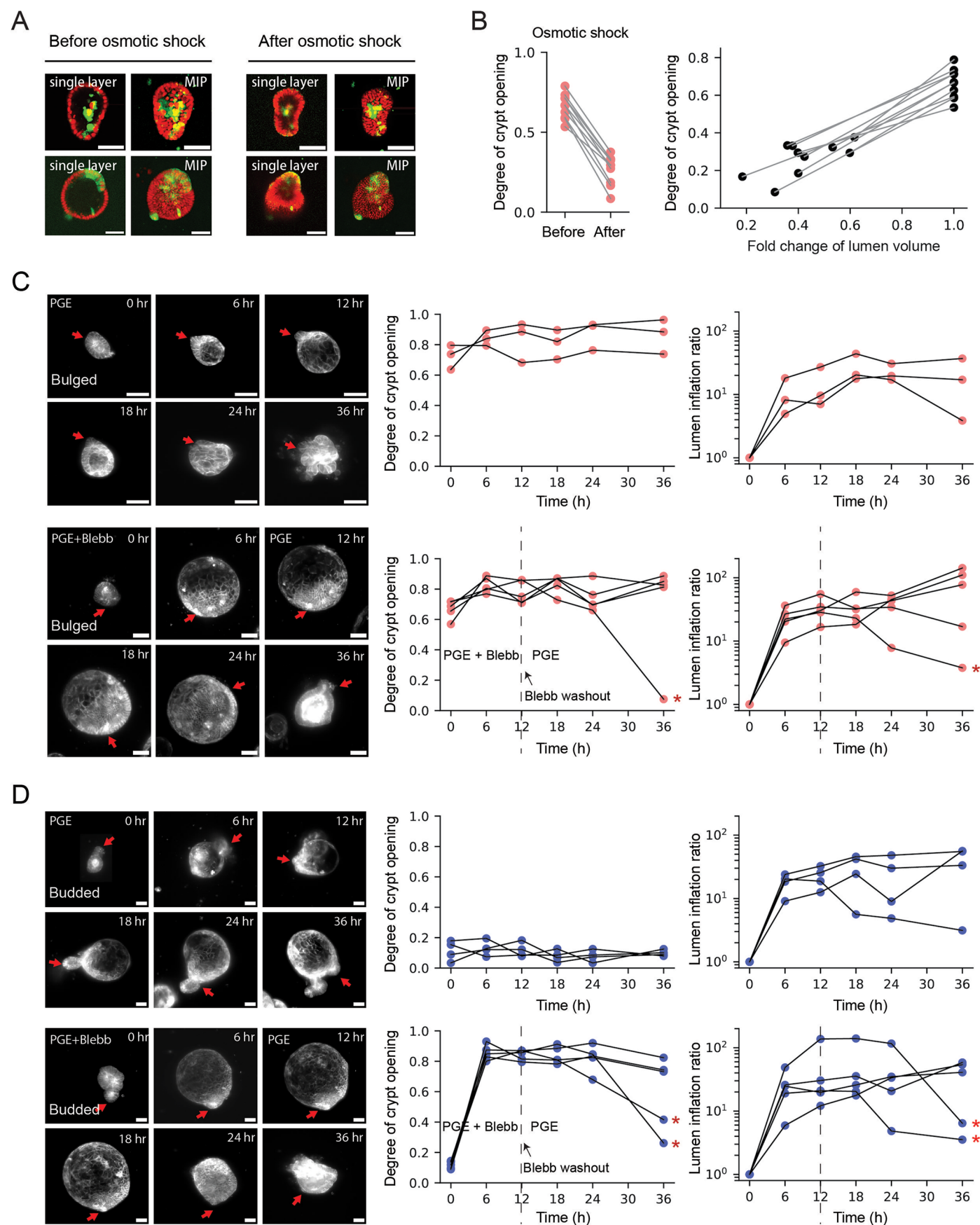


Extended Data Fig. 1 | See next page for caption.

Extended Data Fig. 1 | Cell-type composition in crypts and the relocation of actomyosin. A. Cartoon to show the cell types in intestinal organoid. **B.** Left, representative images for the straining of Lgr5 in both bulged and budded crypts. Cell trace indicates all cells, H2B-iRFP marks cell nuclei and Lgr5-DTR-GFP marks intestinal stem cells. Right, Lgr5⁺ cell numbers are similar in bulged and budded crypts (sample number $N = 18$ (bulged) and $N = 22$ (budded), $p = 0.22$, two-tailed t-test). **C–E.** Representative images for the staining of Lyz (C), YAP (D) and Delta 1 (E) in crypts. Paneth cell numbers are similar in bulged and budded crypts

(sample number $N = 42$ (bulged) and $N = 49$ (budded), $p = 0.48$, two-tailed t-test). **F.** Time-lapse recordings of basal crypt actomyosin relocation during lumen inflation. Red arrows point to the crypt basal surface with increasing Myh-9-GFP intensity. Scale bars: 50 μm . The box-plot elements (in B and C) show the 25% (Q1, lower bound), 50% (median, line within the box) and 75% (Q3, upper bound) quartiles, and the whiskers denote 1.5 \times the interquartile range (minimum = $Q1 - 1.5 \times (Q3 - Q1)$, maximum = $Q3 + 1.5 \times (Q3 - Q1)$) with outliers (rhombuses).

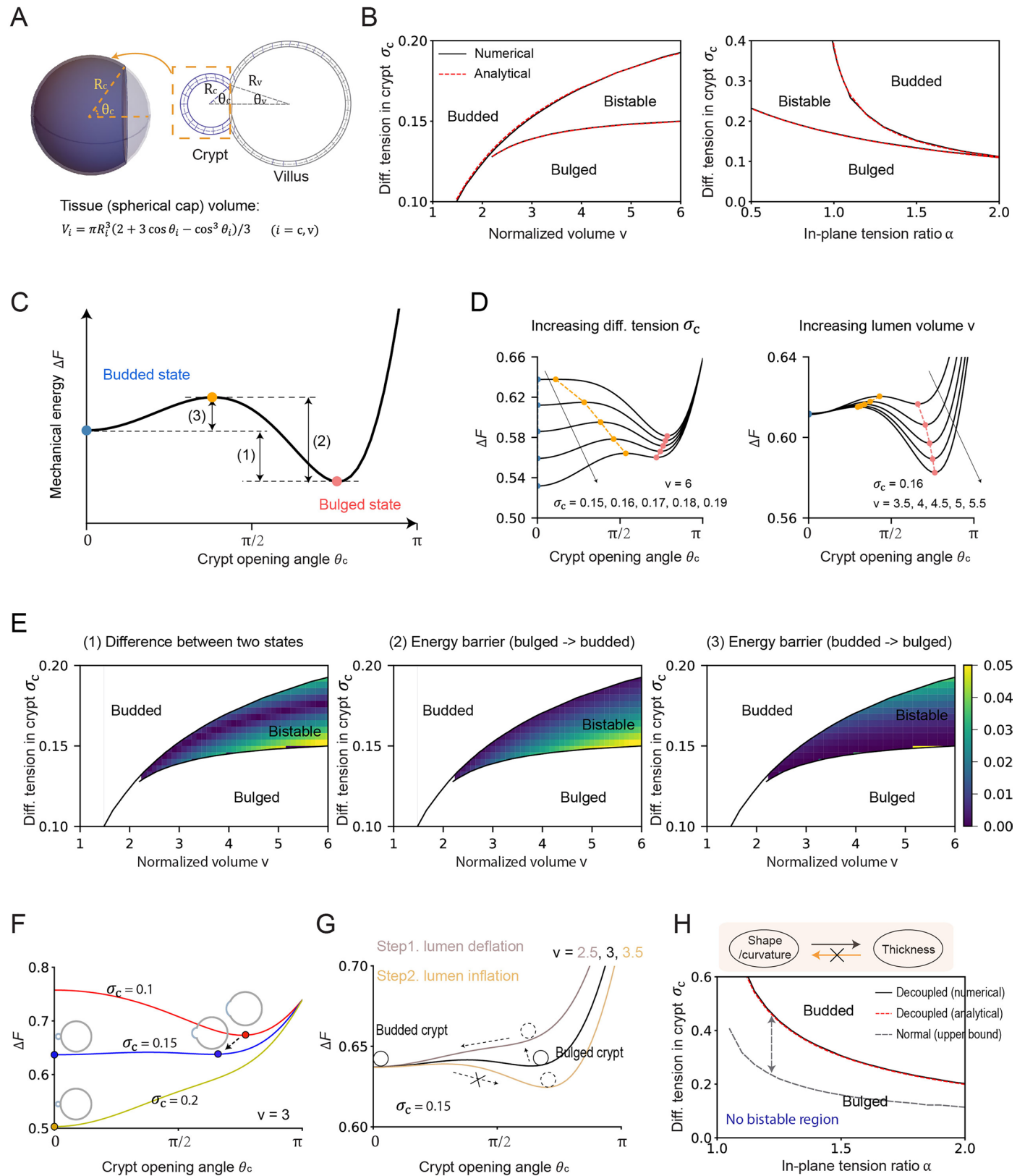




Extended Data Fig. 3 | See next page for caption.

Extended Data Fig. 3 | Crypt morphogenesis with various mechanical perturbations. **A.** Representative images of organoid before and after osmotic shock. **B.** Quantification of the degree of crypt opening and fold changes of lumen volume before and after osmotic shock ($N = 10$). **C, D.** Representative time-lapse images (left), evolution of the degree of crypt opening (middle) and the lumen volume (right) of bulged (C) or budded (D) organoids with two types of treatments: i) PGE treatment alone for 36 hours (see the upper panels

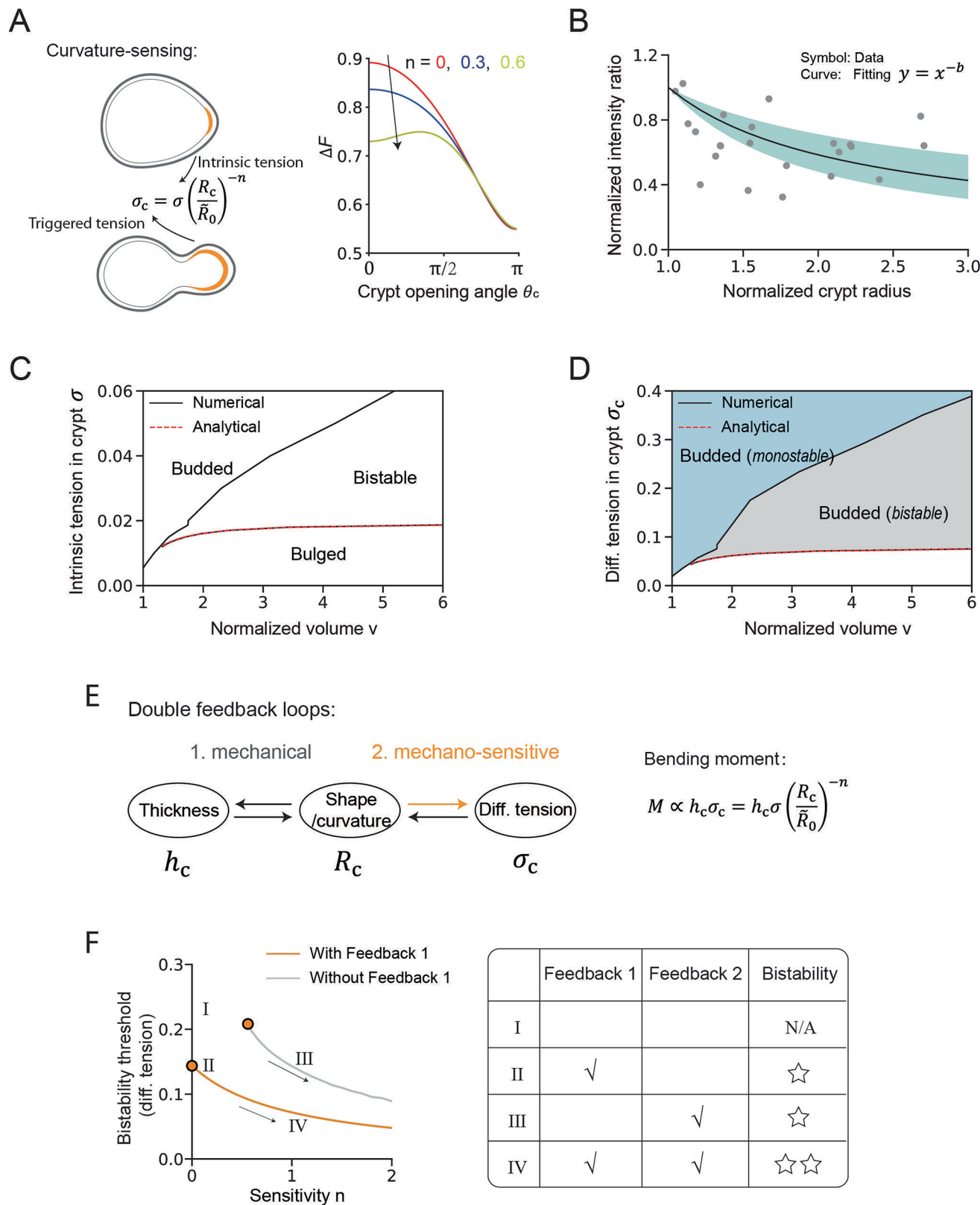
in C and D, with $N = 3$ for bulged samples, and $N = 4$ for budded samples); ii) PGE and Blebbistatin treatments for 12 hours, followed by PGE treatment alone (Blebbistatin being washed out) for another 24 hours (see the lower panels in C and D, with $N = 5$ for both bulged and budded samples). Red arrows indicate the crypts. The red stars next to the last datapoints indicate the samples that show lumen deflate in the late stage, which correlate with late budding. Scale bar: 50 μm .



Extended Data Fig. 4 | See next page for caption.

Extended Data Fig. 4 | Detailed theoretical analysis of crypt morphological bistability without mechano-sensation. **A.** Three-dimensional geometry of intestinal organoid, and basic geometric relations used to establish the model (see SI Note section 1.1 for details). **B.** Comparison between numerical (from the full model) and analytical (from the simplified model) results of phase boundaries in $\sigma_c - \nu$ diagram ($\alpha = 1.2$, left panel) and $\sigma_c - \alpha$ diagram ($\nu = 10$, right panel), showing high consistency. **C.** Schematics of a bistable energy landscape with mechanical energy ΔF as a function of crypt opening degree θ_c . Two local minima respectively correspond to budded ($\theta_c = 0$) and bulged ($\theta_c > 0$) crypt shapes, and we label (1) the energy difference between bulged

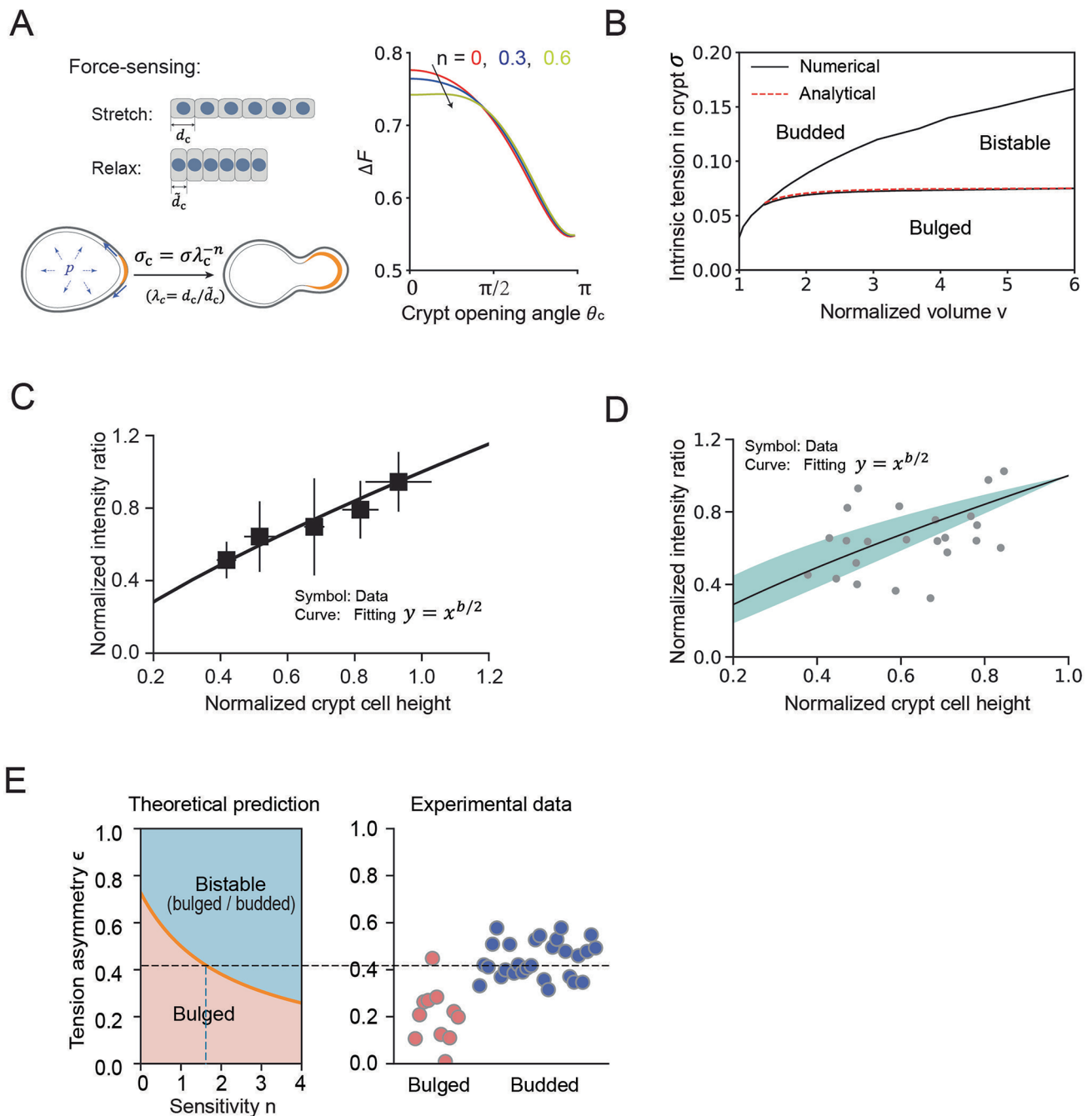
and budded states, (2) the energy barrier for bulged to budded transition, and (3) the energy barrier for budded to bulged transition. **D.** Evolution of energy landscapes for varying differential tension σ_c (left) and lumen volume ν (right). **E.** Distributions of energy barriers in the bistable region of $\sigma_c - \nu$ phase diagram. **F, G.** Variation of the energy landscape indicates the evolution of crypt shape with differential tension σ_c (F) and lumen volume ν (G). **H.** Crypt morphology in $\sigma_c - \alpha$ diagram after decoupling crypt curvature and thickness, and comparison with the original model. Compared to panel B, this shows an absence of bistable region, as well as higher threshold for budding.



Extended Data Fig. 5 | See next page for caption.

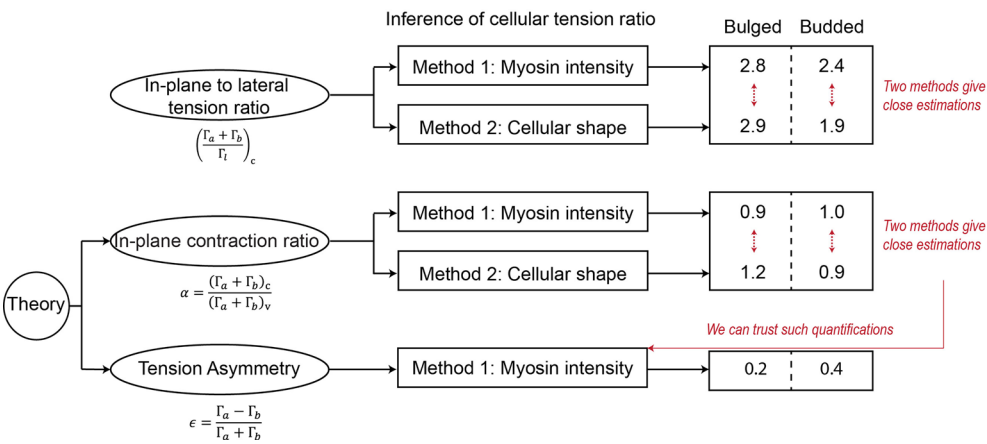
Extended Data Fig. 5 | Detailed analysis of crypt morphological bistability with curvature-sensitivity. We set crypt size $\varphi = 0.1$ and in-plane contraction ratio $\alpha = 1.2$ for all theoretical predictions (based on quantifications in Extended Data Fig. 9 for α and φ , and see SI Note section 3.2 and 4.3 for details). **A.** Left, schematic of the curvature-sensing mechanism, where the total differential tension σ_c is the product of an intrinsic value σ (arising from stem cell fate,²³) as well as a contribution inversely proportional to the crypt radius of curvature R_c with sensitivity n . Right, influence of curvature-sensitivity (n) on the energy landscape ($\sigma = 0.05$, infinite volume), showing that it gives rise to a second minimum. **B.** Fitting of curvature-sensitivity. Apical to basal Myh9–GFP intensity ratio and crypt radius after lumen inflation are normalized by their values before inflation (bulged samples, $N = 24$). Best fit of data and 95% confidence interval are respectively shown as solid line and shaded region. **C, D.** Crypt morphology with

curvature-sensation ($n = 1$) in $\sigma - v$ diagram (C) and corresponding $\sigma_c - v$ diagram showing an enhanced region of bistability (D, compare to Fig. 2a and Extended Data Fig. 4B). **E.** Double feedback loops in crypt morphogenesis. Feedback 1 is the mechanical coupling between epithelial thickness and curvature (see Fig. 2d for schematic), and Feedback 2 is the coupling between crypt tension and deformation (with mechano-sensation, see panel A for schematic). **F.** Evaluation of specific feedback loops that enable crypt bistability (see SI Note section 2.3 for details). Left, bistability threshold of differential tension σ_c without/with the purely mechanical Feedback 1 as well as its dependence on Feedback 2 (mechano-sensation with sensitivity n). Right, summary of the effects of two feedback loops on the size of the bistable region in phase diagram.

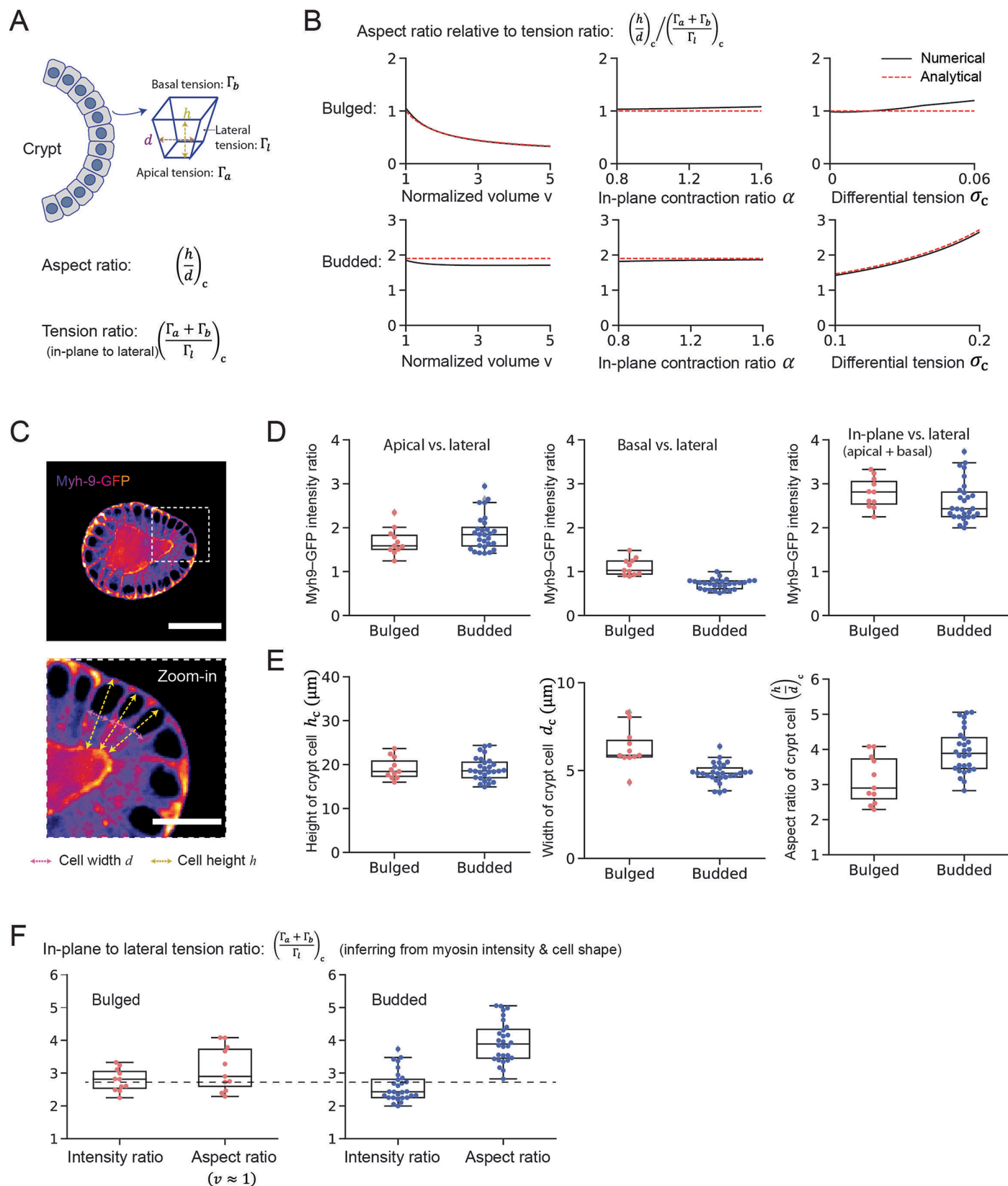
**Extended Data Fig. 6 | Crypt morphological bistability with force-sensitivity.**

A. Left, schematic of force-sensing mechanism, with crypt cell in-plane stretch ratio λ_c defined. Right, influence of force-sensitivity (n) on the energy landscape ($\sigma = 0.1$, infinite volume), showing qualitatively similar features as curvature-sensing. **B.** Phase diagram of crypt morphology with force-sensation. **C, D.** Fitting of force-sensitivity. Apical to basal Myh9–GFP intensity ratio and crypt cell height (or thickness) after lumen inflation are normalized by their values before inflation (bulged samples, $N = 24$). The fitting curve is $y = x^{b/2}$, with the fitting

parameter b used to infer force-sensitivity n . Fittings the mean values (squares, panel C) and raw data (dots, panel D) give similar best-fit values (see SI Note section 4.1 for details). Error bars (panel C) represent SD, the shaded region (panel D) represents 95% confidence interval. **E.** Predicted influence of sensitivity factor n on the bistability threshold of tension asymmetry ϵ , and comparison with experimental data of bulged ($N = 11$) and budded ($N = 28$) samples for the best-fit value $n = 1.7$ from panel C.



Extended Data Fig. 7 | Quantification strategy of mechanical parameters related to cellular tension. Table showing the comparison of different quantification procedures.

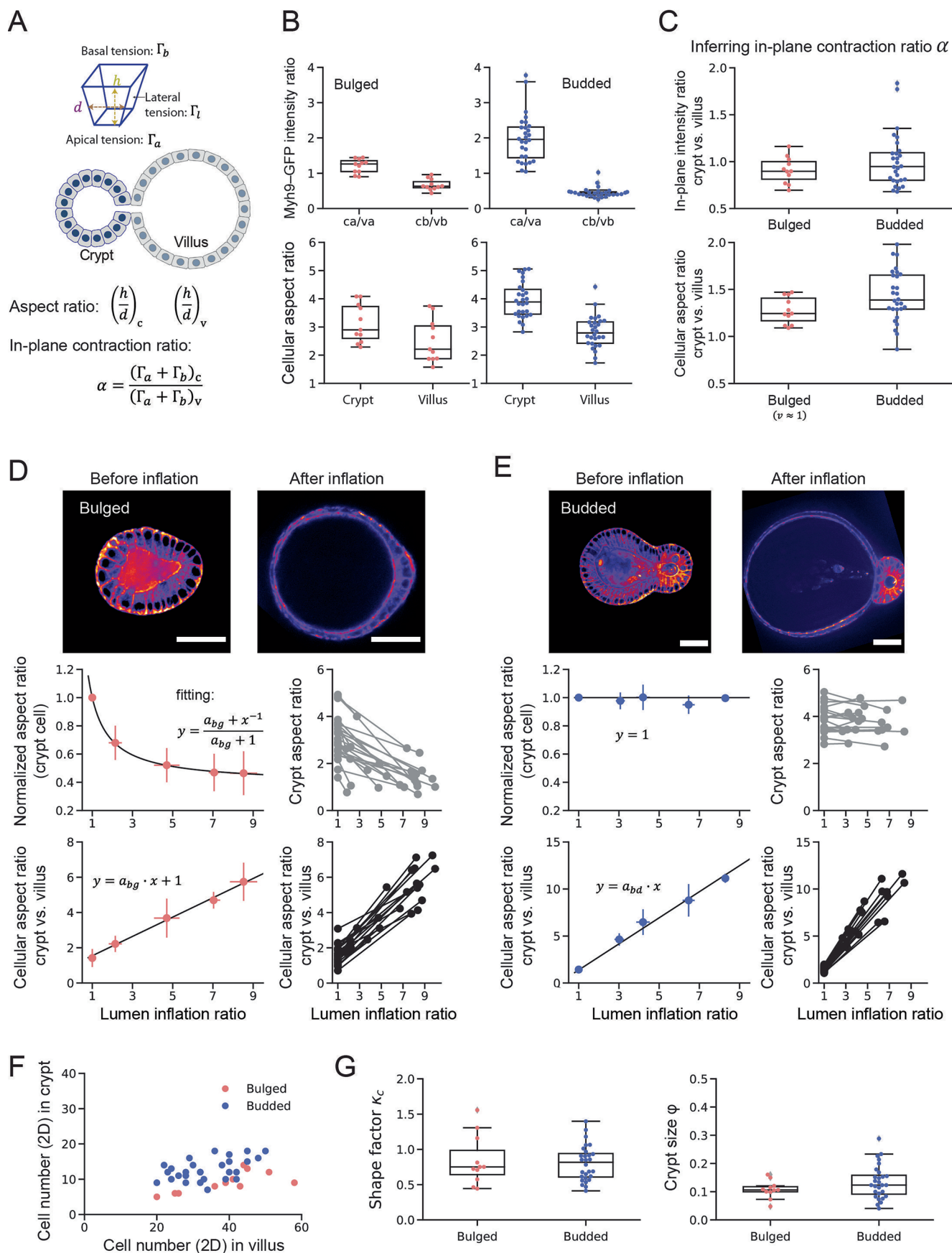


Extended Data Fig. 8 | See next page for caption.

Extended Data Fig. 8 | Link between mechanical and morphometric parameters.

A. Definitions of crypt cellular aspect ratio ($\frac{h}{d}_c$) and in-plane to lateral tension ratio ($\frac{\Gamma_a+\Gamma_b}{\Gamma_l}_c$) (see SI Note section 3.1 for details). **B.** Sensitivity analysis for how model parameters affect the correlation between aspect ratio ($\frac{h}{d}_c$) and in-plane to lateral tension ratio ($\frac{\Gamma_a+\Gamma_b}{\Gamma_l}_c$) in both bulged and budded crypts: the dependence of the normalized value ($\frac{h}{d}_c$) / ($\frac{\Gamma_a+\Gamma_b}{\Gamma_l}_c$) on normalized volume ν (left), in-plane contraction ratio α (middle) and differential tension σ_c (right). We set $\nu = 1$, $\alpha = 1.2$ and $\sigma_c = 0.03$ (bulged) or 0.15 (budded) unless the parameter is varying. **C.** Representative organoid image with Myh-9-GFP staining and extraction of cellular height h and width d . **D.** Quantification of Myh-9-GFP intensity ratio: apical, basal, and in-plane (sum of apical and basal) intensities are normalized by lateral intensity in each crypt (bulged: $N = 11$, budded: $N = 28$).

E. Quantification of cellular height h_c , width d_c and aspect ratio ($\frac{h}{d}_c$) in both bulged and budded crypts (bulged: $N = 11$, budded: $N = 28$). Bulged samples are those after lumen breakage (that is $\nu \approx 1$, also shown in Fig. 2e), and in this state, cellular tension ratio and aspect ratio are expected to share the same value based on sensitive analysis B. **F.** Inference of in-plane to lateral tension ratio ($\frac{\Gamma_a+\Gamma_b}{\Gamma_l}_c$) from corresponding Myh-9-GFP intensity ratio (that is right panel in D) and cellular aspect ratio (based on sensitive analysis B, tension ratio can also be inferred from aspect ratio in panel E). The box-plot elements show the 25% (Q1, lower bound), 50% (median, line within the box) and 75% (Q3, upper bound) quartiles, and the whiskers denote 1.5× the interquartile range (minimum = $Q1 - 1.5 \times (Q3 - Q1)$, maximum = $Q3 + 1.5 \times (Q3 - Q1)$) with outliers (rhombuses). Scale bars: 50 μm (organoid) and 20 μm (magnification).



Extended Data Fig. 9 | See next page for caption.

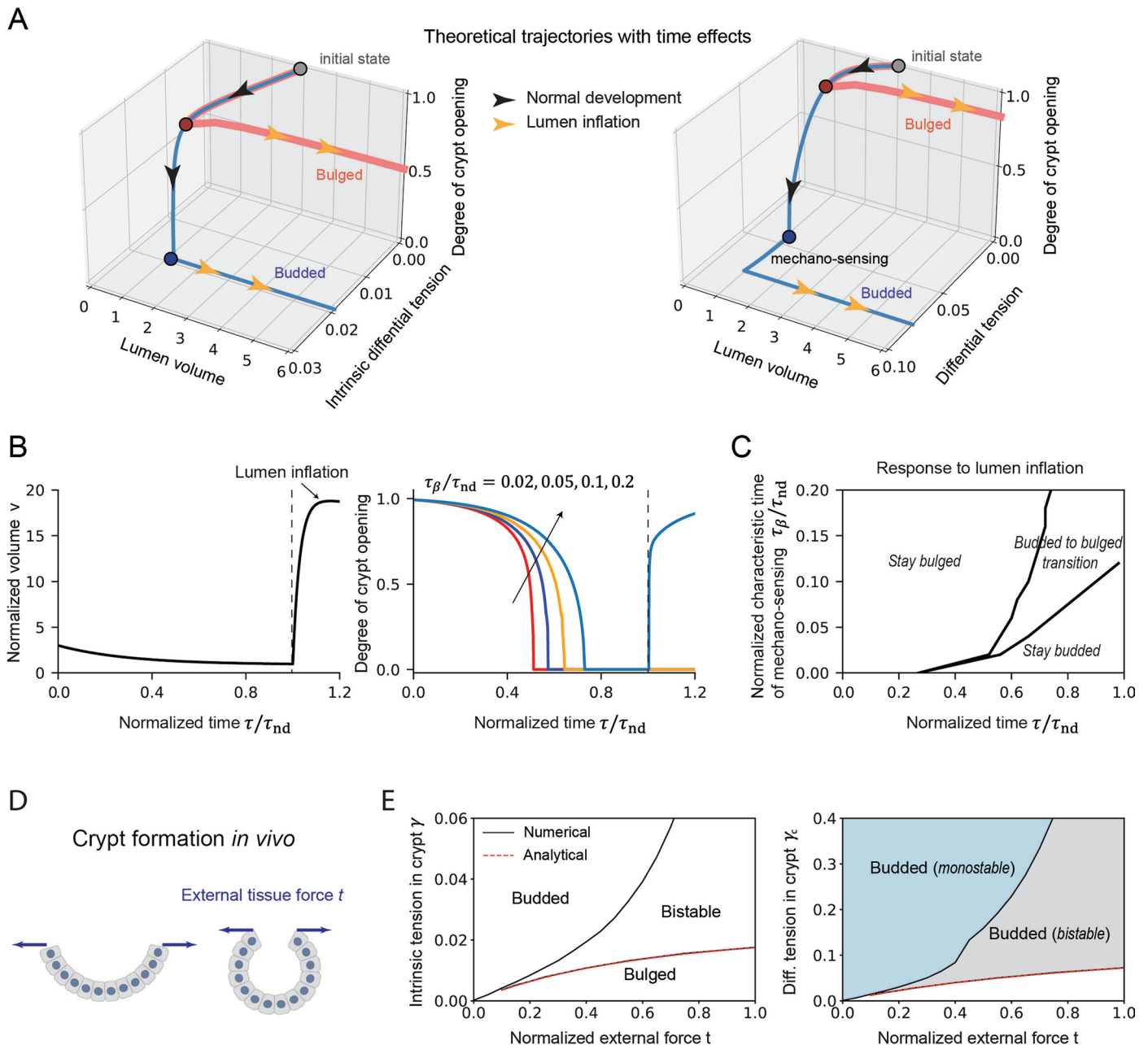
Extended Data Fig. 9 | Quantification of mechanical parameters. A. Definitions of cellular aspect ratios $(\frac{h}{d})_c$ and $(\frac{h}{d})_v$, and in-plane contraction ratio

$$\alpha = \frac{(\Gamma_a + \Gamma_b)_c}{(\Gamma_a + \Gamma_b)_v},$$

with subscripts c and v respectively denoting crypt and villus.

B. Quantification of Myh-9-GFP intensity and cell shape: top, crypt to villus Myh-9-GFP intensity ratios, including crypt apical (ca) to villus apical (va), and crypt basal (cb) to villus basal (vb); bottom, quantification of cellular aspect ratios in crypt $(\frac{h}{d})_c$ and that in villus $(\frac{h}{d})_v$. **C.** Inference of in-plane contraction ratio α from both Myh-9-GFP intensity and cell shape: top, the ratio of in-plane Myh-9-GFP intensities (that is the sum of apical and basal intensities) of crypt to villus cell; bottom, the aspect ratio of crypt to villus cell $(\frac{h}{d})_c / (\frac{h}{d})_v$. In panel B and C, both bulged ($N = 11$) and budded ($N = 28$) samples are quantified. Bulged samples with lumen breakage (labelled as $\nu \approx 1$, also used in Fig. 2e) are chosen to quantify cellular aspect ratio as their cell shapes give direct inference of α (see SI Note section 3.2 for details). **D, E.** Fitting of the lumen inflation-induced morphometric variation with analytic formulae derived from the model. The images (top) show the organoid morphology and cell shape before and after

lumen inflation by PGE treatment. Morphometric variation in cells is tracked by (middle) normalized aspect ratio of crypt cell $(\frac{h}{d})_c^{\text{infl}} / (\frac{h}{d})_c^{\text{ctr}}$ (that is the value after lumen inflation $(\frac{h}{d})_c^{\text{infl}}$ normalized by that before inflation $(\frac{h}{d})_c^{\text{ctr}}$), presented as mean \pm SD, with data of $(\frac{h}{d})_c^{\text{ctr}}$ and $(\frac{h}{d})_c^{\text{infl}}$ shown in the right panel), and (bottom) aspect ratio of crypt to villus cell $(\frac{h}{d})_c / (\frac{h}{d})_v$ (mean \pm SD, with raw data shown in the right panel), in both bulged (panel D, $N = 24$) and budded (panel E, $N = 19$) organoids. **F.** Quantification of cell numbers in crypt and villus cross-sections (2D) from organoid images, which are used to estimate parameters in panel G (see SI Note section 3.3 and 4.3 for details). **G.** Measurement of shape factor κ_c (left) and crypt size ϕ (right) in bulged ($N = 11$) and budded ($N = 28$) crypts. The box-plot elements show the 25% (Q1, lower bound), 50% (median, line within the box) and 75% (Q3, upper bound) quartiles, and the whiskers denote $1.5 \times$ the interquartile range (minimum = $Q1 - 1.5 \times (Q3 - Q1)$, maximum = $Q3 + 1.5 \times (Q3 - Q1)$) with outliers (rhombuses). Scale bars: 50 μm .



Extended Data Fig. 10 | Crypt bistability mechanism: evaluation of time-dependent effects and extension to *in vivo* scenario. **A.** Theoretical trajectories showing the temporal evolution of crypt morphology, differential tension (that is intrinsic tension in the left panel, and total tension in the right one) and lumen volume, specified as normal morphogenesis (black arrows) and lumen inflation of both bulged and budded organoids (orange arrows). **B.** Temporal evolution of lumen volume in normal development and using inflation treatment (left), and corresponding crypt morphologies with various time-scales of mechano-sensing

(right). **C.** Morphological response to lumen inflation for crypts undergoing varying developmental time and showing varying mechano-sensing time-scales. Time-related parameters are normalized by τ_{nd} (overall time of normal bulged-to-budded evolution). **D.** Extension of the model to the *in vivo* setting of an open geometry, where crypt budding can still be modulated and impeded by external force t generated by other tissues (for example villus). **E.** Crypt morphology with curvature-sensation ($n = 1$) in $\sigma - t$ diagram (left) and corresponding $\sigma_c - t$ diagram showing the bistable crypt morphology (right).

Reporting Summary

Nature Portfolio wishes to improve the reproducibility of the work that we publish. This form provides structure for consistency and transparency in reporting. For further information on Nature Portfolio policies, see our [Editorial Policies](#) and the [Editorial Policy Checklist](#).

Statistics

For all statistical analyses, confirm that the following items are present in the figure legend, table legend, main text, or Methods section.

n/a Confirmed

- ☐ ☒ The exact sample size (n) for each experimental group/condition, given as a discrete number and unit of measurement
- ☐ ☒ A statement on whether measurements were taken from distinct samples or whether the same sample was measured repeatedly
- ☐ ☒ The statistical test(s) used AND whether they are one- or two-sided
Only common tests should be described solely by name; describe more complex techniques in the Methods section.
- ☒ ☐ A description of all covariates tested
- ☐ ☒ A description of any assumptions or corrections, such as tests of normality and adjustment for multiple comparisons
- ☒ ☐ A full description of the statistical parameters including central tendency (e.g. means) or other basic estimates (e.g. regression coefficient) AND variation (e.g. standard deviation) or associated estimates of uncertainty (e.g. confidence intervals)
- ☒ ☐ For null hypothesis testing, the test statistic (e.g. F , t , r) with confidence intervals, effect sizes, degrees of freedom and P value noted
Give P values as exact values whenever suitable.
- ☒ ☐ For Bayesian analysis, information on the choice of priors and Markov chain Monte Carlo settings
- ☒ ☐ For hierarchical and complex designs, identification of the appropriate level for tests and full reporting of outcomes
- ☒ ☐ Estimates of effect sizes (e.g. Cohen's d , Pearson's r), indicating how they were calculated

Our web collection on [statistics for biologists](#) contains articles on many of the points above.

Software and code

Policy information about [availability of computer code](#)

Data collection	To collect time-course imaging data, Wako Software Suite (version 2) and custom written segmentation code was used. The code was written in the Liberali lab and implemented with Python 3.8 (relying on multiple open source Python libraries for scientific computing and image analysis). ZEN Black software was used for collecting data of laser nanosurgery. Visview (version 4.4.0.9) was used for collecting confocal imaging data.
Data analysis	To analyze imaging data, Fiji (version 2.9.0) was used. Codes generated and analyzed during the current study are available on https://github.com/fmi-basel/glib-nature_cell_biology2021-materials.git .

For manuscripts utilizing custom algorithms or software that are central to the research but not yet described in published literature, software must be made available to editors and reviewers. We strongly encourage code deposition in a community repository (e.g. GitHub). See the Nature Portfolio [guidelines for submitting code & software](#) for further information.

Data

Policy information about [availability of data](#)

All manuscripts must include a [data availability statement](#). This statement should provide the following information, where applicable:

- Accession codes, unique identifiers, or web links for publicly available datasets
- A description of any restrictions on data availability
- For clinical datasets or third party data, please ensure that the statement adheres to our [policy](#)

All datasets are provided as source Data (excel sheets).

Research involving human participants, their data, or biological material

Policy information about studies with [human participants or human data](#). See also policy information about [sex, gender \(identity/presentation\), and sexual orientation](#) and [race, ethnicity and racism](#).

Reporting on sex and gender

NA

Reporting on race, ethnicity, or other socially relevant groupings

NA

Population characteristics

NA

Recruitment

NA

Ethics oversight

NA

Note that full information on the approval of the study protocol must also be provided in the manuscript.

Field-specific reporting

Please select the one below that is the best fit for your research. If you are not sure, read the appropriate sections before making your selection.

☒ Life sciences ☐ Behavioural & social sciences ☐ Ecological, evolutionary & environmental sciences

For a reference copy of the document with all sections, see [nature.com/documents/nr-reporting-summary-flat.pdf](https://www.nature.com/documents/nr-reporting-summary-flat.pdf)

Life sciences study design

All studies must disclose on these points even when the disclosure is negative.

Sample size

No particular statistical method was used to define sample size. In compound time-course experiments, we assumed a minimum of around 50 organoids at Day4 would be sufficient to recognize differences between control and perturbations based upon historical experiments. Sample size was determined based on previous related studies in the field (Yang et al., 2021, Nature Cell Biology).

Data exclusions

Parameters used to exclude datapoints were defined based on data distributions. Exclusion criteria for segmentation were pre-defined as reported previously (Yang et al., 2021, Nature Cell Biology).

Replication

All experiments were replicated at least twice with similar findings.

Randomization

Samples were randomly assigned.

Blinding

Same investigator performed experiments and data analyses therefore it is not blinding.

Reporting for specific materials, systems and methods

We require information from authors about some types of materials, experimental systems and methods used in many studies. Here, indicate whether each material, system or method listed is relevant to your study. If you are not sure if a list item applies to your research, read the appropriate section before selecting a response.

Materials & experimental systems

n/a	Involved in the study
<input type="checkbox"/>	<input checked="" type="checkbox"/> Antibodies
<input type="checkbox"/>	<input checked="" type="checkbox"/> Eukaryotic cell lines
<input checked="" type="checkbox"/>	<input type="checkbox"/> Palaeontology and archaeology
<input checked="" type="checkbox"/>	<input type="checkbox"/> Animals and other organisms
<input checked="" type="checkbox"/>	<input type="checkbox"/> Clinical data
<input checked="" type="checkbox"/>	<input type="checkbox"/> Dual use research of concern
<input checked="" type="checkbox"/>	<input type="checkbox"/> Plants

Methods

n/a	Involved in the study
<input checked="" type="checkbox"/>	<input type="checkbox"/> ChIP-seq
<input checked="" type="checkbox"/>	<input type="checkbox"/> Flow cytometry
<input checked="" type="checkbox"/>	<input type="checkbox"/> MRI-based neuroimaging

Antibodies

Antibodies used	anti-YAP (Cell signaling technology mAB #14074, clone D8H1X, dilution 1:200), anti-Dll1(R&D Systems AF3970, clone NA (Polyclonal), dilution 1:200), anti-Lysozyme (DAKO A0099, clone NA (Polyclonal), dilution 1:500), Alexa Fluor 488 goat anti rabbit IgG (Thermo fisher scientific B40943, dilution 1:2000), Alexa Fluor 568 donkey anti sheep IgG (Thermo fisher scientific A-21099, dilution 1:2000).
Validation	Validation statements available from manufacturers: anti- YAP (https://www.cellsignal.com/products/primary-antibodies/yap-d8h1x-xp-rabbit-mab/14074), anti-Dll1 (https://www.rndsystems.com/cn/products/mouse-rat-dll1-antibody_af3970), anti-Lysozyme (https://www.labome.com/product/Dako/A0099.html).

Eukaryotic cell lines

Policy information about [cell lines and Sex and Gender in Research](#)

Cell line source(s)	Wnt3a L-cells , gift from Novartis.
Authentication	The cell line used was not authenticated.
Mycoplasma contamination	The cell line is tested negative with mycoplasma contamination.
Commonly misidentified lines (See ICLAC register)	No commonly misidentified lines in this lab.

Plants

Seed stocks	<i>Report on the source of all seed stocks or other plant material used. If applicable, state the seed stock centre and catalogue number. If plant specimens were collected from the field, describe the collection location, date and sampling procedures.</i>
Novel plant genotypes	<i>Describe the methods by which all novel plant genotypes were produced. This includes those generated by transgenic approaches, gene editing, chemical/radiation-based mutagenesis and hybridization. For transgenic lines, describe the transformation method, the number of independent lines analyzed and the generation upon which experiments were performed. For gene-edited lines, describe the editor used, the endogenous sequence targeted for editing, the targeting guide RNA sequence (if applicable) and how the editor was applied.</i>
Authentication	<i>Describe any authentication procedures for each seed stock used or novel genotype generated. Describe any experiments used to assess the effect of a mutation and, where applicable, how potential secondary effects (e.g. second site T-DNA insertions, mosaicism, off-target gene editing) were examined.</i>